

# THE ASTROPHYSICAL $r$ -PROCESS: A COMPARISON OF CALCULATIONS FOLLOWING ADIABATIC EXPANSION WITH CLASSICAL CALCULATIONS BASED ON NEUTRON DENSITIES AND TEMPERATURES

C. FREIBURGHHAUS,<sup>1</sup> J.-F. REMBGES, T. RAUSCHER, E. KOLBE,<sup>1</sup> AND F.-K. THIELEMANN<sup>1,2</sup>  
Departement für Physik und Astronomie, Universität Basel, Klingelbergstrasse 82, CH-4056 Basel, Switzerland

AND

K.-L. KRATZ AND B. PFEIFFER

Institut für Kernchemie, Universität Mainz, Fritz-Strassmann-Weg 2, D-55099 Mainz, Germany

AND

J. J. COWAN<sup>1</sup>

Department of Physics and Astronomy, University of Oklahoma, Norman, OK 73019

Received 1997 November 5; accepted 1998 November 30

## ABSTRACT

The rapid neutron-capture process ( $r$ -process) encounters unstable nuclei far from  $\beta$ -stability. Therefore its observable features, like the abundances, witness (still uncertain) nuclear structure as well as the conditions in the appropriate astrophysical environment. With the remaining lack of a full understanding of its astrophysical origin, parameterized calculations are still needed. We consider two approaches: (1) the classical approach is based on (constant) neutron number densities  $n_n$  and temperatures  $T$  over duration timescales  $\tau$ ; (2) recent investigations, motivated by the neutrino wind scenario from hot neutron stars after a supernova explosion, followed the expansion of matter with initial entropies  $S$  and electron fractions  $Y_e$  over expansion timescales  $\tau$ . In the latter case the freezeout of reactions with declining temperatures and densities can be taken into account explicitly.

We compare the similarities and differences between the two approaches with respect to resulting abundance features and their relation to solar  $r$ -process abundances, applying for the first time different nuclear mass models in entropy-based calculations. Special emphasis is given to the questions of (a) whether the same nuclear properties far from stability lead to similar abundance patterns and possible deficiencies in (1) and (2), and (b) whether some features can also provide clear constraints on the astrophysical conditions in terms of permitted entropies,  $Y_e$  values, and expansion timescales in (2). This relates mostly to the  $A < 110$  mass range, where a fit to solar  $r$ -abundances in high-entropy supernova scenarios seems to be hard to attain. Possible low-entropy alternatives are presented.

*Subject headings:* nuclear reactions, nucleosynthesis, abundances — supernovae: general

## 1. INTRODUCTION

The question of whether we understand fully all astrophysical sites leading to an  $r$ -process is not a settled one. It is generally assigned to high-entropy ejecta of Type II supernovae (SNe II), the events accompanying the deaths of massive stars and formation of neutron stars (high-entropy ejecta; see, e.g., Woosley et al. 1994; Takahashi, Witt, & Janka 1994). But Galactic evolution and the delayed emergence of  $r$ -process matter indicate also that probably only SNe II with long progenitor evolution timescales in the mass range  $\sim 8$ – $10 M_\odot$  can be responsible (Cowan, Thielemann, & Truran 1991; Mathews, Bazan, & Cowan 1992; McWilliam et al. 1995). On the other hand, neutron star mergers or still other low-entropy sites are not necessarily excluded (e.g., Lattimer et al. 1977; Meyer 1989; Eichler et al. 1989; Rosswog et al. 1999). Both these environments provide or can possibly provide high neutron densities and high temperatures that ensure an  $(n, \gamma)$ – $(\gamma, n)$  equilibrium in each isotopic chain before the final decline of densities and temperatures during the explosion. Models that try to

explain the whole  $r$ -process composition by low neutron density ( $< 10^{20} \text{ cm}^{-3}$ ) and temperature ( $< 10^9 \text{ K}$ ) environments, such as explosive He burning in massive stars (Thielemann, Arnould, & Hillebrandt 1979), were clearly invalidated by Blake et al. (1981) and Cowan, Cameron, & Truran (1985), as they worked only with excessive initial abundances of  $^{13}\text{C}$ .

For the  $r$ -process source discussion it is also helpful to ask which abundance pattern we need to explain: (1) the present *isotopic*  $r$ -process abundances in the solar system or (2) *element* abundance observations of low-metallicity stars. The latter are very old stars and display with their unchanged surface abundances the composition of the interstellar medium early in Galactic evolution. This relates to the question whether the solar  $r$ -abundances represent an average of many different contributions or whether each of these contributions is already identical with the solar pattern, in terms of elements as well as isotopes. The observations of low-metallicity stars are all consistent with the solar  $r$ -process pattern, and the *relative* abundances among heavy elements apparently do now show any time evolution. It does not matter whether stars of  $[\text{Fe}/\text{H}] = \log [(\text{Fe}/\text{H})/(\text{Fe}/\text{H})_\odot] = -3.1$  (CS 22892–052),  $-2.7$  (HD 115444),  $-2.5$  (HD 122563), or  $-1.7$  (HD 126238) are observed (Snedden et al. 1996; Cowan et al. 1997), at least for elements heavier than Ba, as long as the Galaxy is younger

<sup>1</sup> Institute for Theoretical Physics, University of California at Santa Barbara, Santa Barbara, CA 93106-4030.

<sup>2</sup> Visiting Scientist, Physics Division, Oak Ridge National Laboratory, Oak Ridge, TN 37831-6371.

than the lifetime of low- and intermediate-mass stars that contribute to *s*-process abundances. The analysis of Ba line profiles in several metal-poor stars, making use of hyperfine splitting which causes different line widths and depths for odd and for even isotopes (François & Gacquer 1998), showed that also the ratio of odd to even isotopes agrees with a solar *isotopic r*-process distribution. This, plus the reproduction of the third *r*-process peak (Os, Ir, Pt), suggests strongly that (at least beyond Ba) all contributing astrophysical events have a solar *r*-process composition, opposite to claims of others (Goriely & Arnould 1997).

The stellar source, however, is not conclusive yet, and schematic models are still needed. On average, Type II supernovae produce Fe to intermediate-mass elements in ratios within a factor of 3 of solar (Gratton & Sneden 1991; Nissen et al. 1994; Thielemann, Nomoto, & Hashimoto 1996). If they were also responsible for the *r*-process, the same limits should apply. But the observed bulk *r*-process/Fe ratios vary widely in low-metallicity stars. For example, CS 22892 – 052 has an *r*/Fe ratio that is 30 times larger than solar! This may argue for another almost pure *r*-process nucleosynthesis origin, different from that of supernovae.

The observations discussed above led to the conclusions that the many events contributing during galactic evolution are apparently very similar and produce the same relative *r*-process abundances. However, even the same astrophysical site has varying conditions in different ejected mass zones. This naturally guides toward a multievent model (where all events are close to identical); however, each event displays a multicomponent (i.e., superposition) behavior, where a component is defined by a combination of neutron number density, temperature, and duration time, or more physically for an adiabatic expansion, entropy, the total proton-to-nucleon ratio  $Y_e = \langle Z/A \rangle$ , and an expansion timescale. The physical conditions should vary smoothly, as expected from a single astrophysical event, but different from the assumptions of Goriely & Arnould (1996).

In the present paper we want to compare results of such parameterized calculations being based on conditions expected in a high-entropy wind in SNe II, making use of initial entropy  $S$ ,  $Y_e$ , and an expansion timescale  $\tau$ , with findings of our previous site-independent, classical studies based on (constant) neutron number densities  $n_n$  and temperatures  $T$  over a duration time  $\tau$ . The question is whether earlier conclusions from calculations within the classical approach can be generalized also for high-entropy supernova environments. Finally, we consider low-entropy/high-density conditions, in the past often related to “cold” decompression of neutron star matter, and compare their results to those of the classical approach as well. This should provide a good understanding of the way in which nuclear physics enters the abundance pattern for different types of astrophysical environments.

In § 2 we will summarize our present knowledge of calculations within a site-independent, classical approach, based on  $n_n$ ,  $T$ , and  $\tau$ , where the waiting-point approximation, i.e., an  $(n, \gamma)$ – $(\gamma, n)$  equilibrium, could be applied. Entropy-based calculations are presented in § 3. First, we give a detailed account of the nuclear input, especially aspects of our new cross section calculations required for the full network treatment without applying the waiting-point approximation. It follows the framework of our calculations and an overview of one entropy sequence at a fixed  $Y_e$ , dis-

playing the typical properties of an  $\alpha$ -rich freezeout from charged particle reactions and subsequent *r*-process nucleosynthesis. Variations of these properties with  $Y_e$  and expansion timescales  $\tau$  are also discussed. A comparison of entropy superpositions with those of the site-independent, classical approach is provided in § 4 for high-entropy and low-entropy environments. The possible role of neutrino-induced reactions on heavy nuclei is discussed as well. In § 5 we summarize the options of how to overcome problems of abundance deficiencies in comparison with solar *r*-process abundances. They provide, on the one hand, constraints on nuclear physics far from stability, as well as on environment conditions that are very similar to those obtained from our previous site-independent, classical studies within the waiting-point approximation. On the other hand, we discuss how abundance features in the nuclear mass range  $A = 80$ – $110$ , which are inherent in high-entropy neutrino wind models, can be circumvented and present various possible solutions (and speculations).

## 2. THE SITE-INDEPENDENT, CLASSICAL APPROACH

### 2.1. The Method

The classical approach makes use of constant neutron densities  $n_n$ , temperatures  $T$ , and duration times  $\tau$ . As we choose here only conditions that fulfill an equilibrium between neutron captures and photodisintegrations ( $n_n > 10^{20} \text{ cm}^{-3}$  and  $T > 10^9 \text{ K}$  [Cameron, Cowan, & Truran 1983; Bouquelle et al. 1996; Goriely & Arnould 1996], which cause reaction timescales as short as  $\approx 10^{-4} \text{ s}$ ), a full nuclear reaction network need not be solved (e.g., Cowan et al. 1991; Kratz et al. 1993) and the freezeout is assumed instantaneously at  $t = \tau$ , just requiring to follow subsequent  $\beta$ -decay processes.

In an  $(n, \gamma)$ – $(\gamma, n)$  equilibrium (the waiting-point approximation) the maximum abundances in isotopic chains occur at the same neutron separation energy, which is determined by a combination of the neutron number density  $n_n$  and the temperature  $T$  in an astrophysical environment. Connecting the abundance maxima in isotopic chains defines the so-called *r*-process path. The paths responsible for the solar *r*-process abundances encounter highly neutron-rich, unstable nuclei, located 15–35 units away from  $\beta$ -stability with neutron separation energies of the order of  $S_n = 2$ – $4 \text{ MeV}$ . These are predominantly nuclei not accessible in laboratory experiments to date, with exceptions in the  $A = 80$  and  $130$  peaks, as discussed in Kratz et al. (1993). The dependence on nuclear masses or mass model predictions enters via  $S_n$ . The  $\beta$ -decay properties along contour lines of constant  $S_n$  toward heavy nuclei (see, e.g., Fig. 1) are responsible for the resulting abundance pattern. The buildup of heavy nuclei is governed by the abundance distribution in each isotopic chain from  $(n, \gamma)$ – $(\gamma, n)$  equilibrium and by effective decay rates  $\lambda_\beta^Z$  of isotopic chains. The environment properties  $n_n$  and  $T$  (defining the  $S_n$  of the path) and the duration time  $\tau$  predict the abundances. In case the duration time  $\tau$  is larger than the longest half-lives encountered in such a path, a steady flow of  $\beta$ -decays will also follow, making the abundance ratios independent of  $\tau$ .

One has to recognize a number of idealizations in this picture. It assumes a constant  $S_n(n_n, T)$  over a duration time  $\tau$ . Then the nuclei will still be existent in the form of highly

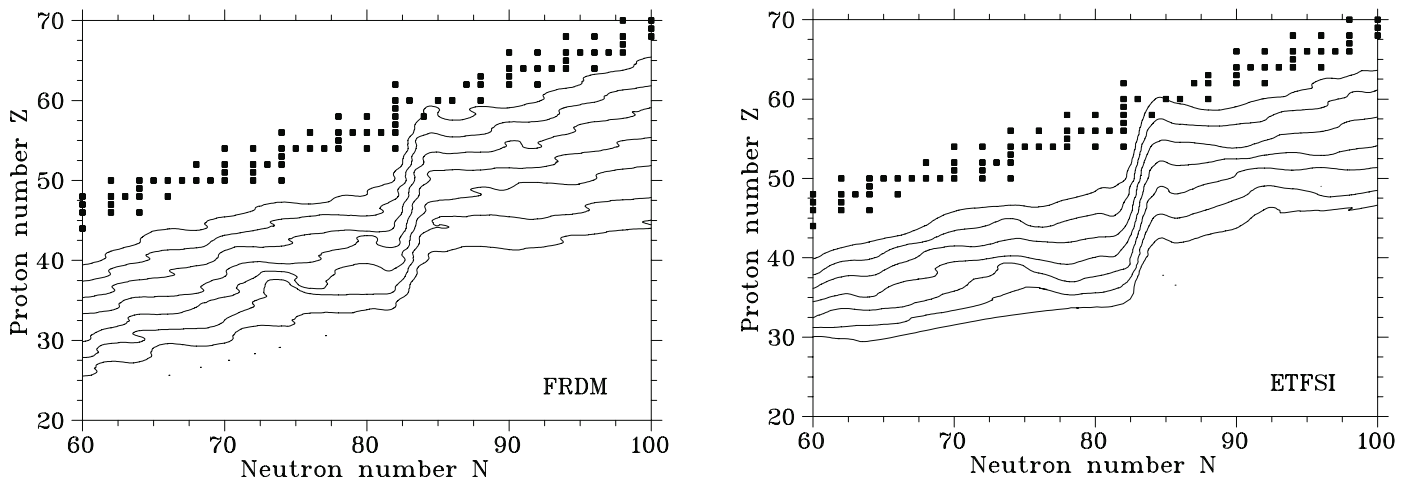


FIG. 1.—Contour plots of constant neutron separation energies in the  $80 \leq A \leq 140$  mass region for the FRDM mass model (Möller et al. 1995) and the ETFSI mass model (Aboussir et al. 1995) at  $S_n = 1, 2, 3, \dots, 7$  MeV for even- $N$  isotopes. The saddle point behavior before the shell closure at  $N = 82$ , causes the deep trough before the peak at  $A = 130$  (see upper part of Fig. 3) as the step from the abundance maximum of an isotopic chain  $Z$  to  $Z + 1$  can cause a large jump in  $N$  or equivalently  $A$ , leading to a large number of unpopulated mass numbers  $A$ .

unstable isotopes, which have to decay back to  $\beta$ -stability. In reality  $n_n$  and  $T$  will be time dependent. As long as both are high enough to ensure the waiting-point approximation, this is not a problem because the system will immediately adjust to the new equilibrium, and only the new  $S_n(n_n, T)$  is important. This leads, however, to a scaling of the duration time  $\tau$ , as paths at different  $S_n$  values experience different  $\beta$ -decay half lives. The more prominent question is whether the decrease from equilibrium conditions in  $n_n$  and  $T$  (freezeout), which initially ensure the waiting-point approximation, down to conditions where the competition of neutron captures and  $\beta$ -decays has to be taken into account explicitly, will affect the abundances strongly.

When following the strategy outlined above, the analysis of the solar system isotopic  $r$ -process abundance pattern showed that a minimum of three components with different  $S_n$  values, characterizing different  $r$ -process paths, were necessary for correctly reproducing the three peaks at  $A \simeq 80, 130$ , and  $195$  and the abundances in between (Thielemann et al. 1993; Kratz et al. 1993). For a temperature of  $T = 1.35 \times 10^9$  K these three components correspond to neutron number densities of order  $n_n = 10^{20}$ ,  $10^{22}$ , and  $10^{24}$  g cm $^{-3}$  (the combination of both choices being equivalent to  $r$ -process paths with  $S_n = 3.81, 3.28$ , and  $2.75$  MeV for even- $N$  isotopes) with time durations (of the time-dependent calculations not assuming a steady flow) of 1.2, 1.6, and 2.15 s and respective weights in a superposition of 96:31:10. The “low- $A$  wings” of the peaks (when making use of experimental  $\beta$ -decay properties at the magic neutron numbers  $N = 50$  and  $82$ ), as well as the abundance pattern down to the next peak, could be reproduced, even with the assumption of a steady flow of  $\beta$ -decays. This indicates that the astrophysical duration timescales  $\tau$  are large in comparison to most of the  $\beta$ -decay half-lives encountered and only comparable to the longest half-lives in the peaks (where the path comes closest to stability) which control the leaking out to larger  $A$ -values.

As we expect in a single astrophysical event smooth changes over mass zones and not a superposition of very specific conditions, we chose superpositions of 10 components within the same  $n_n(S_n, T)$  boundaries and equidistant steps in  $\log n_n$ , according to duration timescales and

superposition weights consistent with the three-component fit for a temperature of  $T = 1.35 \times 10^9$  K:

$$\begin{aligned} \tau(n_n) &= 6.97 \times 10^{-2} n_n^{0.062}, \\ w(n_n) &= 8.36 \times 10^6 n_n^{-0.247}. \end{aligned} \quad (1)$$

Such a continuous superposition of components with varying  $n_n$ ,  $T$ , or  $S_n(n_n, T)$  (rather than only three), with equidistant steps in  $S_n$  between 2 and 4 MeV and  $\tau$  between 1 and 2.5 s, led to a slight, but not dramatic, change/improvement of the abundance curve.

In Figure 2 we show the behavior of the quantity  $\lambda_\beta^Z Y_{(Z)}$  for the different sets of component superpositions.  $Y_{(Z)}$  denotes the total abundance  $Y_{(Z)} = \sum_A Y_{(Z,A)}$  and  $\lambda_\beta^Z = (1/Y_{(Z)}) \sum_A Y_{(Z,A)} \lambda_\beta^{Z,A}$  the effective decay rate of an entire isotopic chain. The quantity  $\lambda_\beta^Z Y_{(Z)}$  measures the total feeding of isotopic chain  $Z + 1$ . The constancy of  $\lambda_\beta^Z Y_{(Z)}$  shows the degree to which a steady flow of  $\beta$ -decays is attained. We see that the three-component fit results in essentially horizontal lines in between magic numbers. At magic neutron numbers, the steady flow breaks down due to the long half-lives at the top of the kinks at magic numbers in an  $S_n$ -contour line (see also Fig. 1). This is an obvious signature of nuclear shell closures. The 10-component superposition, being closer to a continuous behavior, leads to a slight tilt of the  $\lambda_\beta^Z Y_{(Z)}$  lines, but not a strong change. This is very similar to the steady-flow behavior of neutron captures in the  $s$ -process (see Käppeler, Beer, & Wisshak 1989), where the quantity  $\sigma_{h,\gamma}^A Y_{(A)}$  testifies to the existence of a steady flow of neutron captures in between magic neutron numbers. The 13-component fit did not make use of a finer grid but extended the  $n_n(S_n, T)$  range with the same step size in  $\log n_n$  to larger  $n_n$  values (smaller  $S_n$  values) with the same laws for  $\tau(n_n)$  and  $w(n_n)$ , showing that for such conditions also the actinides can be produced.

## 2.2. Nuclear Structure Signatures

When the calculations of Kratz et al. (1993) were supplemented by use of the most modern mass formula results (Finite Range Droplet Model [FRDM] by Möller et al. 1995 and Extended Thomas-Fermi with Strutinsky Integral [ETFSI] by Aboussir et al. 1995), instead of using a some-

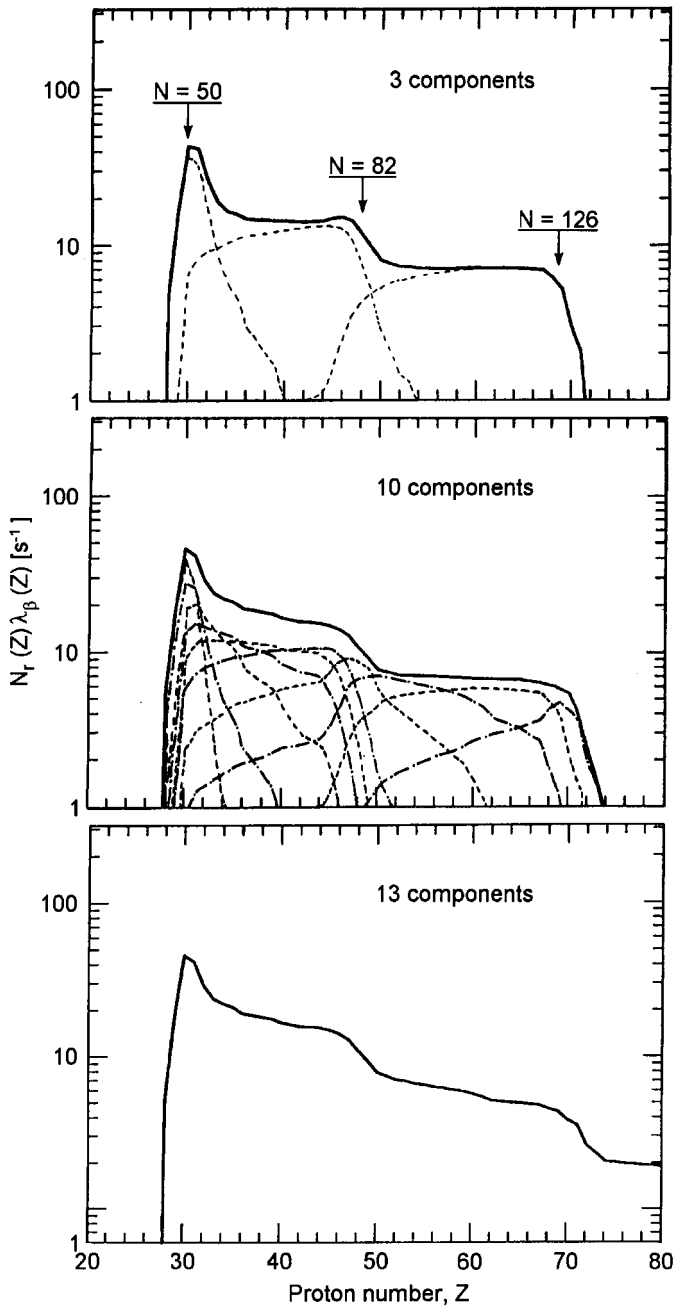


FIG. 2.—Steady flow test for 3, 10, and 13 component fits. The three components (sets of  $n_n$  and  $T$ ) correspond to different  $r$ -process paths, characterized by those  $S_n$  values which reproduced the “low- $A$  wings” of the three peaks at  $A \simeq 80, 130$ , and  $195$  and the abundance pattern down to the next peak in Kratz et al. (1993), when making use of the waiting-point approximation and assuming a steady flow of  $\beta$ -decays between isotopic chains. Dropping the latter assumption and performing time-dependent calculations over timescales of 1–2.5 s leads nevertheless exactly to a steady flow in between magic neutron numbers, as demonstrated by the constancy of  $\lambda_\beta^r Y_{(Z)}$ , because the duration timescales  $\tau$  are large in comparison to most of the  $\beta$ -decay half-lives encountered and only comparable to the longest half-lives in the peaks, where the path comes closest to stability and the steady flow breaks down (*top panel*). A more continuous 10-component superposition, which gives a slight improvement of the overall abundance fit, keeps essentially the steady flow behavior with a small tilt of the  $\lambda_\beta^r Y_{(Z)}$  curve, similar to what is observed in the  $s$ -process  $\sigma_{n,\gamma}^A T_{(A)}$  curve (*middle panel*). When adding three components with equidistant steps in  $S_n$  with smaller neutron separation energies, the same behavior also extends to larger mass numbers, enabling also the production of actinide nuclei (*bottom panel*).

what dated but still quite successful droplet model by Hilf, von Groote, & Takahashi (1976), we could show that abundance troughs appeared before (and after) the 130 and 195 abundance peaks, due to the behavior of the  $S_n$  contours of these mass models (Thielemann et al. 1994; Chen et al. 1995; Kratz 1995). The location in  $N$  of an  $r$ -process path with a given  $S_n$  does not behave smoothly as a function of  $Z$ . Figure 1 indicates a sudden jump to the position of the magic neutron number, where the contour lines show a saddle-point behavior for the FRDM as well as ETFSI mass models in the  $S_n = 2$ –4 MeV range. The population gap of nuclei as a function of  $A$  leads after decay to the abundance trough of Figure 3.

Additional tests were performed in order to see how this pattern could be avoided with different nuclear structure properties far from stability. The problem could be resolved (Chen et al. 1995) if for very neutron-rich nuclei the shell gap at the magic neutron number  $N = 82$  is less pronounced (i.e., quenched) than predicted by the global macroscopic-microscopic mass models (Möller et al. 1995; Aboussir et al. 1995). In light nuclei, the quenching of shells in neutron-rich isotopes is well established by now and is a long-studied effect (Campi et al. 1975; Orr 1991; Fukunishi, Otsuka, & Sebe 1992; Sorlin et al. 1993; Ibbotson et al. 1998). Experiments close to the  $N = 82$  closed shell seem to indicate shell quenching also for this mean region (Hoff et al. 1996; Zhang et al. 1997). Hartree-Fock-Bogoliubov calculations (Dobaczewski et al. 1996) with a specific Skyrme force, as well as relativistic mean field calculations (Lalazissis, Vretenar, & Ring 1998), seem to have exactly the expected effect on the  $r$ -process path and the resulting abundance curve (see Chen et al. 1995). This effect was also confirmed by Pearson, Nayak, & Goriely (1996), when the ETFSI mass formula was phenomenologically quenched in a similar way to the HFB results. It leads to a very good agreement with solar  $r$ -abundances (see Fig. 3 and Pfeiffer, Kratz, & Thielemann 1997). Hence, a continuous experimental investigation of shell quenching along the  $N = 50$  and 82 shell toward more neutron-rich nuclei (and approaching the  $r$ -process path for  $N = 126$ ) is a highly desirable goal in order to test the nuclear structure responsible for the solar abundances of heavy nuclei.

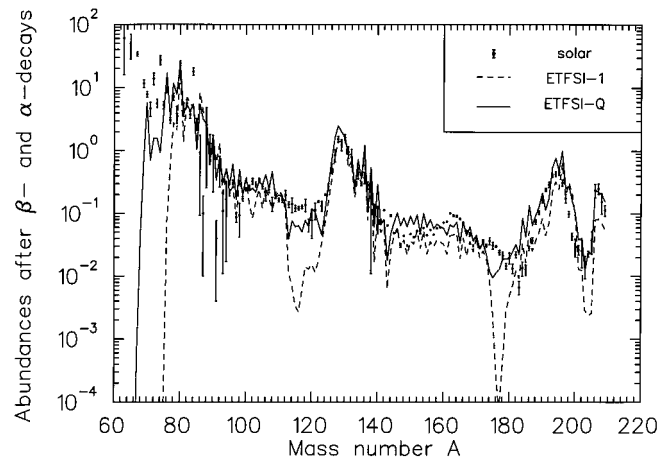


FIG. 3.—Fits to  $r$ -process abundances (Käppeler et al. 1989) obtained with 10 equidistant  $S_n(n_n, T)$  components from 2 to 4 MeV (Cehn et al. 1995). The quenching of the  $N = 82$  shell gap by the ETFSI-Q mass model of Pearson, Nayak, & Goriely (1996) leads to a filling of the abundance troughs and to a better overall reproduction of the heavy mass region.

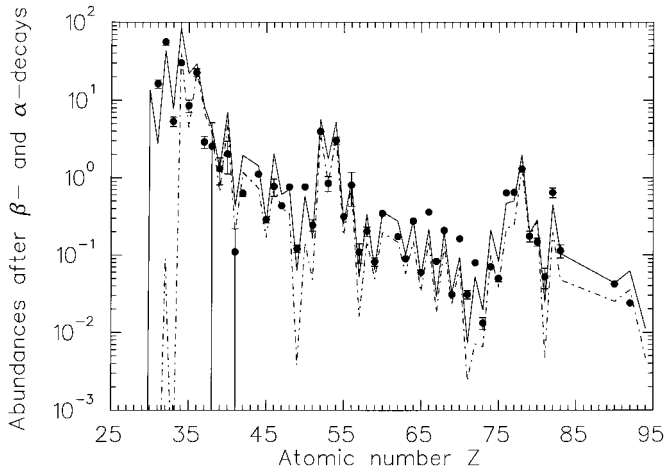


FIG. 4.—Element abundances (summed over isotopic chains) from a superposition of classical  $r$ -process calculations (see text) for two different mass models. Results obtained with ETFSI masses are displayed as a dashed line, ETFSI-Q results are displayed by a solid line. The element abundances reflect the features of isotopic abundances from Fig. 3. Also for elements one sees a deviation from solar  $r$ -abundances (error bars) for the ETFSI mass model, when a smooth superposition of components is utilized.

Summarizing the results of the classical, site-independent investigations, we are led to the following conclusions: under assumption of (1) an  $(n, \gamma)$ – $(\gamma, n)$  equilibrium, as expected from all astrophysical  $r$ -process sites, at least during their initial phases, (2) an instantaneous freezeout of capture and photodisintegration reactions, and (3) a smooth superposition of astrophysical conditions of  $n_n$  and  $T$ , as expected from a single astrophysical site (supported by observations of old stars), we obtain abundance features with present-day mass models that indicate the necessity of nuclear shell quenching for nuclei far from stability. It remains to be seen whether calculations not based on the classical approach and somewhat relaxing assumption (2) lead to similar conclusions.

On a different note we would like to point out that the differences showing up in isotopic abundances for the two different mass models shown in Figure 3 also appear in element abundance plots. This can be seen in Figure 4, where the isotopic abundances of Figure 3 are summed up to obtain element abundances (for the solar abundances as well as for the two mass models). One clearly recognizes the differences in the abundance peaks and in the troughs before the  $A \sim 130$  and 195 peaks. Only in limited mass regions between peaks an element pattern similar to a solar pattern can be obtained with nonsolar isotopic abundances (see Goriely & Arnould 1997; Sneden et al. 1996; Cowan et al. 1997).

### 3. AN ENTROPY-BASED APPROACH

#### 3.1. The Method

There are two aspects that have to be considered when trying to relate the site-independent, classical studies of § 2 to astrophysics: (1) what kind of environments can produce the required conditions, and (2) do the nuclear structure conclusions drawn with the sudden freezeout approximation from the  $(n, \gamma)$ – $(\gamma, n)$  equilibrium stay valid for actual time-dependent freezeouts encountered in a specific environment? We will return to these questions after having

discussed the details of the calculations, which are motivated by recent  $r$ -process studies (Woosley et al. 1994; Takahashi et al. 1994; Qian et al. 1996; Qian & Woosley 1996; Hoffman, Woosley, & Qian 1997) for the hot environment in the innermost ejecta of Type II supernovae, also called the neutrino wind. These are the layers heated by neutrino emission to a specific temperature/entropy and evaporating from the hot, collapsed proto-neutron star. Such calculations obtained neutron separation energies  $S_n$  of the  $r$ -process path in the range of 2–4 MeV (Takahashi et al. 1994), in agreement with Kratz et al. (1993). Whether the entropies required for these conditions can really be attained in supernova explosions has still to be verified.

In order to test whether explosion entropies can be translated into  $n_n$  and  $T$  (or  $S_n$ ) of the site-independent, classical approach, we performed a parameter study based on entropies  $S$  and the total proton-to-nucleon ratio  $Y_e$  (which measures the neutron richness of the initial composition), in combination with an expansion timescale (for the radius of a blob of matter starting with initial entropy  $S$ ) of typically 0.05 s (Takahashi et al. 1994), and varied nuclear properties (i.e., mass models) as in § 2. The calculations follow a hot blob of matter with entropy  $S$ : (1) initially it consists of neutrons, protons, and some  $\alpha$ -particles in a ratio given by nuclear statistical equilibrium (NSE) for a specific  $Y_e$ , and expands adiabatically and cools; (2) the nucleons and  $\alpha$ -particles combine to heavier nuclei (typically Fe group), with some neutrons and  $\alpha$ -particles remaining; (3) for high entropies an  $\alpha$ -rich freezeout from charged particle reactions occurs for declining temperatures (Woosley, Arnett, & Clayton 1973; Thielemann, Hashimoto, & Nomoto 1990), producing nuclei in the mass range  $A \approx 80$ –100; (4) finally, these nuclei with total abundance  $Y_{\text{seed}}$  can capture the remaining neutrons  $Y_n$  and undergo an  $r$ -process. We consider a simple model of an adiabatically expanding homogeneous mass zone with increasing volume  $V(t)$  and an expansion timescale relevant to the supernova problem. This approximation is justified by hydrodynamic and semi-analytic simulations of the evolution of the high-entropy wind (Mayle & Wilson 1990; Wittl, Janka, & Takahashi 1994; Janka & Müller 1996; Qian & Woosley 1996). The calculations were performed for a grid of entropies  $S$  and electron fractions  $Y_e$  ( $S = 3, 10, 20, 30, \dots, 390 k_B \text{ baryon}^{-1}$  and  $Y_e = 0.29, 0.31, \dots, 0.49$ ). Preliminary results were presented in Freiburghaus et al. (1997) and Thielemann et al. (1997).

Parameter studies of a similar type were performed by Meyer et al. (1992), Howard et al. (1993), Hoffman, Woosley, & Qian (1997), Meyer & Brown (1997a), and Meyer & Brown (1997b). However, their main emphasis was put on a first exploration of the scenario, i.e., whether and how it is possible to synthesize even the heaviest elements up to the  $A = 195$  abundance peak, as suggested by Woosley & Hoffman (1992); what entropies are needed for it; and whether the main features of solar  $r$ -process abundances could be reproduced. Here we focus on a detailed analysis of the abundance features, explore different nuclear mass models and their impact, and concentrate on the difficult mass range  $A < 120$ . Different mass zones have different initial entropies, which leads therefore to a superposition of different contributions in the total ejecta. This will be discussed in § 4.

The electron abundance  $Y_e$  and the entropy  $S$  are convenient parameters for the thermodynamic and nucleo-

synthesis evolution of an adiabatically expanding hot bubble. The entropy at high temperatures is mainly radiation-dominated. We must, however, take into account also electrons and positrons at sufficiently high temperatures, comparable in energy to or larger than the particle rest mass. A formulation which covers the extreme cases (pure radiation or also ultrarelativistic electrons and positrons) has been introduced in the formalism of Wittl et al. (1994):

$$S = \frac{4}{3} a \frac{T^3}{\rho} \left[ 1 + \frac{7}{4} f(T_9) \right] = 1.21 \frac{T_9^3}{\rho_5} \left[ 1 + \frac{7}{4} f(T_9) \right], \quad (2)$$

where we made use of a simple fit formula for  $f(T_9)$  ranging between 0 and 1 (H.-T. Janka 1998, private communication; see also Fig. 2 in Wittl et al. 1994);  $S$  is the entropy in  $k_B$  per baryon,  $\rho_5$  the density in units of  $10^5 \text{ g cm}^{-3}$ , and  $T_9$  the temperature in units of  $10^9 \text{ K}$ . An adiabatic expansion follows:

$$T(t) = T_0 \left[ \frac{V_0}{V(t)} \right]^{\gamma-1}, \quad (3)$$

where  $\gamma$  is the adiabatic exponent,  $T(t)$  is the temperature at time  $t$ ,  $V(t)$  is the volume of the mass zone at time  $t$ , and  $T_0$  and  $V_0$  are the initial values of temperature and volume.  $V(t)$  was modeled as an expanding sphere with radius  $R(t)$  and a constant expansion velocity  $\dot{R}$ :

$$V(t) = \frac{4}{3} \pi R(t)^3 = \frac{4}{3} \pi (R_0 + \dot{R}t)^3. \quad (4)$$

Equation (3) with  $\gamma = 4/3$  leads to

$$T(t) = T_0 \left( \frac{R_0}{R_0 + \dot{R}t} \right). \quad (5)$$

The density can be expressed via equation (2). The initial values of  $R_0$ ,  $T_0$ , and the expansion velocity  $\dot{R}$  were chosen to be  $R_0 = 130 \text{ km}$ ,  $T_0 = 9 \times 10^9 \text{ K}$ , and  $\dot{R} = 4500 \text{ km s}^{-1}$ , similar to supernova conditions (Mayle & Wilson 1990; Wittl et al. 1994; Janka & Müller 1996). The choice of  $R_0$  and  $\dot{R}$  is equivalent to the definition of an expansion timescale  $\tau$ , which we define via  $T(\tau) = T_0/e$ , leading to

$$\tau = \frac{R_0(e-1)}{\dot{R}}. \quad (6)$$

An expansion velocity of  $4500 \text{ km s}^{-1}$  corresponds to a timescale of  $\tau = 50 \text{ ms}$ . To test the sensitivity of the results, we also performed calculations with a timescale of  $\tau = 150 \text{ ms}$ . Effects of different expansion timescales are discussed in § 3.5.

### 3.2. Nuclear Input

For each pair of parameters  $Y_e$  and  $S$ , the calculations were followed with a full nuclear (charged particle) network. At the initial temperature  $T_9 = 9$ , a nuclear statistical equilibrium is guaranteed. It is thus permitted to start with an arbitrary composition. For simplicity we chose just neutrons and protons in the correct ratio required by the corresponding  $Y_e$ . The detailed nuclear network which includes all charged particle- and neutron-induced reactions is given in Table 1. The reaction rate library was the same as described in Thielemann et al. (1996), i.e., thermonuclear rates using the Hauser-Feshbach formalism (Thielemann, Arnould, & Truran 1987), experimental charged particle

TABLE 1  
DIMENSIONS OF THE CHARGED  
PARTICLE NETWORK

$Z$	$A_{\min}$	$A_{\max}$
H.....	1	3
He.....	3	6
Li.....	6	9
Be.....	7	12
B.....	8	14
C.....	10	18
N.....	11	21
O.....	13	22
F.....	15	25
Ne.....	17	29
Na.....	20	34
Mg.....	20	37
Al.....	22	40
Si.....	25	41
P.....	28	44
S.....	29	47
Cl.....	32	50
Ar.....	33	53
K.....	36	58
Ca.....	37	59
Sc.....	40	64
Ti.....	41	65
V.....	44	68
Cr.....	46	69
Mn.....	48	74
Fe.....	50	75
Co.....	53	78
Ni.....	54	80
Cu.....	57	85
Zn.....	58	86
Ga.....	62	94
Ge.....	63	97
As.....	64	100
Se.....	66	103
Br.....	68	106
Kr.....	70	109
Rb.....	73	112
Sr.....	75	117
Y.....	77	120
Zr.....	80	121
Nb.....	83	122
Mo.....	85	123
Tc.....	88	126
Ru.....	89	129
Rh.....	90	136
Pd.....	93	139

rates from Caughlan & Fowler (1988), neutron-induced rates from Bao & Käppeler (1987), and extensions toward the proton and neutron drip lines from van Wormer et al. (1994) and Rauscher et al. (1994).

The entropies utilized in the present study are larger than  $0.15 k_B \text{ baryon}^{-1}$ . This relates to a density  $\rho < 10^8 \text{ g cm}^{-3}$  at  $T_9 = 5$  and causes a so-called  $\alpha$ -rich freezeout, as at these low densities the isotopes below the  $A = 5$  and 8 gaps of stable nuclei cannot stay in equilibrium with heavier nuclei via the triple- $\alpha$  or  $\alpha\alpha n$  reactions during the expansion and cooling (Woosley et al. 1973; Thielemann et al. 1990). This causes a large remaining mass fraction of  ${}^4\text{He}$  when charged particle reactions freeze out. Before charged particle freezeout, a large quasi-equilibrium (QSE) group [being in  $(n, \gamma)$ - $(\gamma, n)$ ,  $(p, \gamma)$ - $(\gamma, p)$  as well as  $(\alpha, \gamma)$ - $(\gamma, \alpha)$  equilibrium]

involves all heavy nuclei. This ensured that in the large charged particle network the upper boundary at Pd ( $A < 120$ ) was never reached. After charged particle freezeout, when only  $(n, \gamma)$ – $(\gamma, n)$  equilibria remain in place, matter can progress to heavier nuclei via  $\beta$ -decays between isotopic chains, which was modeled by the *r*-process network to follow the further evolution. The transition was determined when the  $\alpha$  abundance became asymptotically constant (we made use of the criterion  $\Delta Y_\alpha/Y_\alpha < 10^{-5}$  per time step). The amount of subsequent *r*-processing depends on the available number of neutrons per heavy nucleus:  $Y_{\text{seed}} = \sum_{A>4} Y_{(Z,A)}$ . In case the  $Y_n/Y_{\text{seed}}$  ratio was too small for a subsequent *r*-process, only the  $\beta$ -decays back to the valley of  $\beta$ -stable nuclei were taken into account.

The *r*-process network extended from S ( $Z = 16$ ) to Pb ( $Z = 82$ ). Fission was neglected. Both restrictions are justified, as we only tested conditions for which nuclei up to the third *r*-process peak ( $A = 195$ ) are produced, neglecting higher entropies which also produce the actinides. Neutron capture rates were calculated with a new version of the statistical model code SMOKER (Rauscher, Thielemann, & Kratz 1997), which applies an improved excitation energy-dependent level density treatment. The  $\beta^-$  rates came, similar to our discussions in § 2, either from experimental data or from QRPA calculation by Möller, Nix, & Kratz (1997), based on the finite-range droplet model (FRDM). The same procedure was followed for different mass models, the droplet model by Hill et al. (1976) and the ETFSI model by Aboussir et al. (1995). Thus, we included for the first time in such dynamic calculations consistently recalculated data sets for the neutron capture cross sections and not only a change of the  $Q$ -values for the calculation of the reverse photodisintegration rates. Therefore, we have also for these full-network calculations the choice of three mass models (FRDM, ETFSI, and Hilf), similar to § 2. Only the choice of the third model differs, but it has features similar to the model ETFSI- $Q$  used in § 2, as it does not show abundance deficiencies in the mass range  $110 < A < 125$  (see Kratz et al. 1993). Different data sets of  $\beta$ -decay properties also exist for the three mass models discussed above (Pfeiffer & Kratz 1996). However, since very far from stability the theoretical half-lives turned out to be quite similar (within less than a factor of 2; see also Fig. 19 in Kratz et al. 1993), for simplicity the above-mentioned  $\beta^-$ -rates based on FRDM masses were always used.

### 3.3. A Detailed Entropy Sequence

Charged particle and subsequent *r*-process calculations were performed for the large grid of entropies  $S$  and electron fractions  $Y_e$ , given in § 3.1, and two different expansion timescales. For a general understanding of the nucleosynthesis in high-entropy environments (and its possible deficiencies), we show here the detailed results for one entropy sequence at a fixed  $Y_e = 0.45$ . The main features of the abundance patterns are very similar for different  $Y_e$  values. We will discuss variations in  $Y_e$  in the next subsection

The entropies considered here extend from  $S = 3$  to  $S = 350 k_B \text{ baryon}^{-1}$ . At  $S = 3$ , which is close to a normal freezeout requiring  $S < 0.15$  (see discussion in § 3.2), iron group elements are the most abundant ones along a line given by  $Y_e = \langle Z/A \rangle$  in the nuclear chart. At this low entropy the density is relatively high (see eq. [2]). This ensures that most of the  $\alpha$ -particles can recombine through

the  $3\alpha$  and the  $\alpha\alpha n$  [ ${}^4\text{He}(\alpha, \gamma){}^8\text{Be}(n, \gamma){}^9\text{Be}$ ] reaction sequences, bridging the  $A = 5$  and 8 gaps of unstable nuclei and permitting that essentially all nuclei can recombine to Fe group nuclei, as expected in a full NSE or normal freezeout from explosive Si burning. As a consequence, only a negligible amount of neutrons, protons, and  $\alpha$ -particles remain at the freezeout of charged particle reactions, and the number of free neutrons per heavy nucleus ( $Y_n/Y_{\text{seed}}$ ) is very small, about  $10^{-7}$ .

The following considerations give a rough estimate of the type of heavy nuclei that result from an  $\alpha$ -rich freezeout, occurring at higher entropies. We consider the given  $Y_e = Y_{e,\text{global}}$  being composed of two QSE groups, the group of light elements (neutrons, protons, and  $\alpha$ -particles) and a group of heavy nuclei. We replace the sum over heavy nuclei by an average heavy nucleus. Neutrons do not contribute, because  $Z_n = 0$ , and protons can be neglected after an  $\alpha$ -rich freezeout for  $Y_e < 0.5$ . This leads to

$$\begin{aligned} Y_{e,\text{global}} &= \sum_{\text{light}} Z_i Y_i + \sum_{\text{heavy}} Z_i Y_i \\ &\approx \frac{2}{4} X_\alpha + Z_{\text{heavy}} \frac{X_{\text{heavy}}}{A_{\text{heavy}}} \\ &= 0.5 X_\alpha + Y_{e,\text{heavy}} (1 - X_\alpha - X_n). \end{aligned} \quad (7)$$

Solving this equation for  $Y_{e,\text{heavy}}$  results in

$$Y_{e,\text{heavy}} = \frac{Y_{e,\text{global}} - 0.5 X_\alpha}{1 - X_\alpha - X_n}, \quad (8)$$

which indicates the  $Y_e$  line on which to expect the peak abundances after the  $\alpha$ -rich freezeout (see also Hoffman et al. 1997). The  $\alpha$ -rich freezeout involves a heavy QSE group, where nuclei are also in  $(\alpha, \gamma)$ – $(\gamma, \alpha)$  equilibrium:  $n_\alpha \langle \sigma v \rangle_{\alpha, \gamma} Y_{(Z,A)} = \lambda_{\gamma, \alpha} Y_{(Z+2, A+4)}$ . Making use of this equation and the relation between photodisintegrations and capture reactions due to detailed balance (Fowler, Caughlan, & Zimmermann 1967) leads to

$$\begin{aligned} \frac{Y_{(Z+2, A+4)}}{Y_{(Z,A)}} &= n_\alpha \frac{G_{(Z+2, A+4)}}{G_{(Z,A)}} \left( \frac{A+4}{4A} \right)^{3/2} \left( \frac{2\pi\hbar^2}{m_u k_B T} \right)^{3/2} \\ &\times \exp \left( \frac{S_\alpha(A+4)}{k_B T} \right), \end{aligned} \quad (9)$$

$$S_\alpha = f(n_\alpha, T) = \frac{T_0}{11.605} \ln \left( \frac{3.16 \times 10^6 T_0^{3/2}}{\rho_5 X_\alpha} \right), \quad (10)$$

when inserting  $Y(Z+2, A+4) \approx Y(Z, A)$  at the maximum of nuclei located in an  $\alpha$ -chain.

Similar to the discussion of the  $(n, \gamma)$ – $(\gamma, n)$  equilibrium in § 2, a given  $\alpha$  number density and temperature cause an abundance maximum [where  $Y_{(Z,A)} \approx Y_{(Z+2, A+4)}$ ] at a specific  $\alpha$  separation energy. Knowing the temperature and  $\alpha$  number density at charged particle freezeout automatically gives the information where to find the maximum abundance of heavy nuclei at the intersection of  $Z/A = Y_{e,\text{heavy}}$  and  $S_\alpha(n_\alpha, T)$ . This analysis can be easily undertaken with the aid of equations (8) and (10), as long as the neutron mass fraction, the  $\alpha$  mass fraction, and the density and temperature are known at the freezeout of charged particle reactions.

For entropies between  $S = 10$  and  $S = 80$  the most remarkable feature of the abundance patterns is the sharp

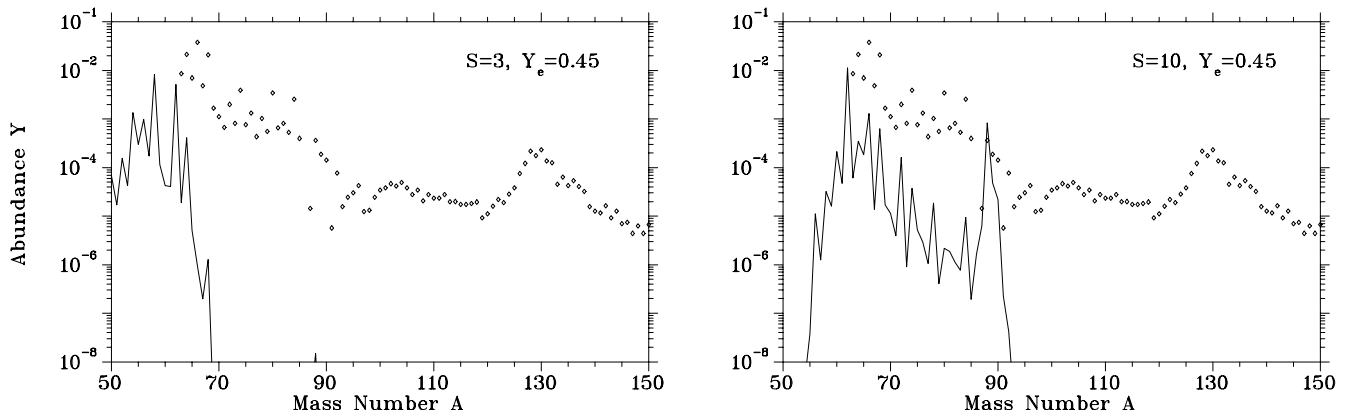


FIG. 5.—First part of the entropy sequence at a fixed  $Y_e = 0.45$ . For this example ETFSI masses are used. The maximum abundances shift from the Fe group peak to a broader distribution with the formation of an  $A \approx 90$  peak.

peak at  $A = 90$  (see Figs. 5 and 6). We find values of  $Y_{e,\text{heavy}}$  in the range 0.446–0.410 and  $S_\alpha \approx 5.5\text{--}6.5$  MeV when making use of equations (8) and (10). This includes typical freezeout quantities of  $T_0 \approx 2.5$ ,  $\rho = (12\text{--}5) \times 10^4 \text{ g cm}^{-3}$  and  $X_\alpha = 0.07\text{--}0.44$ . For  $Y_{e,\text{heavy}}$  lines in the nuclear chart between 0.410 and 0.446 such  $S_\alpha$  values are located at the closed neutron shell  $N = 50$  and give rise to nuclei in the range  $A = 85\text{--}90$  (see Fig. 13 in Möller et al. 1997 for  $Q_\alpha \approx -6$  MeV and the discussion of overproduction of, e.g.,  $^{88}\text{Sr}$ ,  $^{89}\text{Y}$ , and  $^{90}\text{Zr}$  in Woosley & Hoffman 1992; Hoffman et al. 1996, 1997). After the charged particle freezeout, there are

essentially no neutrons available for neutron captures in this range of entropies. This abundance behavior is typical for an  $\alpha$ -rich freezeout at lower entropies and occurs at every  $Y_e$ . The location and structure of the peak can vary, as we will show below.

Entropies up to 130–140 still give small amounts of free neutrons after an  $\alpha$ -rich freezeout. The  $S_\alpha$  values remain in the same range, and  $Y_{e,\text{heavy}}$  goes down to 0.38–0.37, due to increasing  $X_\alpha$  up to 0.5–0.6 and decreasing freezeout densities (see Fig. 7), corresponding to intersections with  $S_\alpha \approx 6$  MeV contour lines at  $A = 100\text{--}110$ . This moves the peak

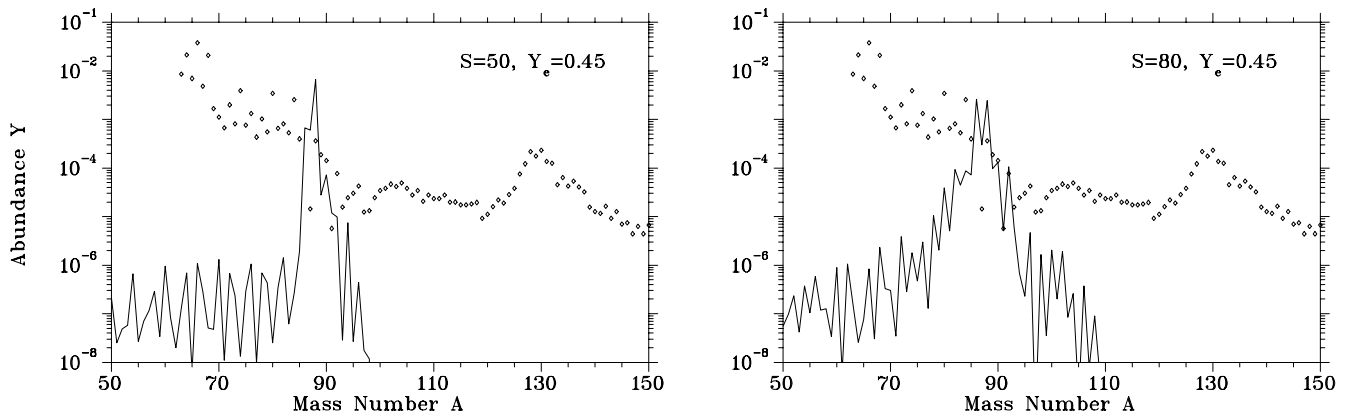


FIG. 6.—Same as Fig. 5 but for higher entropies. A strong peak at  $A \approx 90$ , ( $N \approx 50$ ) is synthesized.

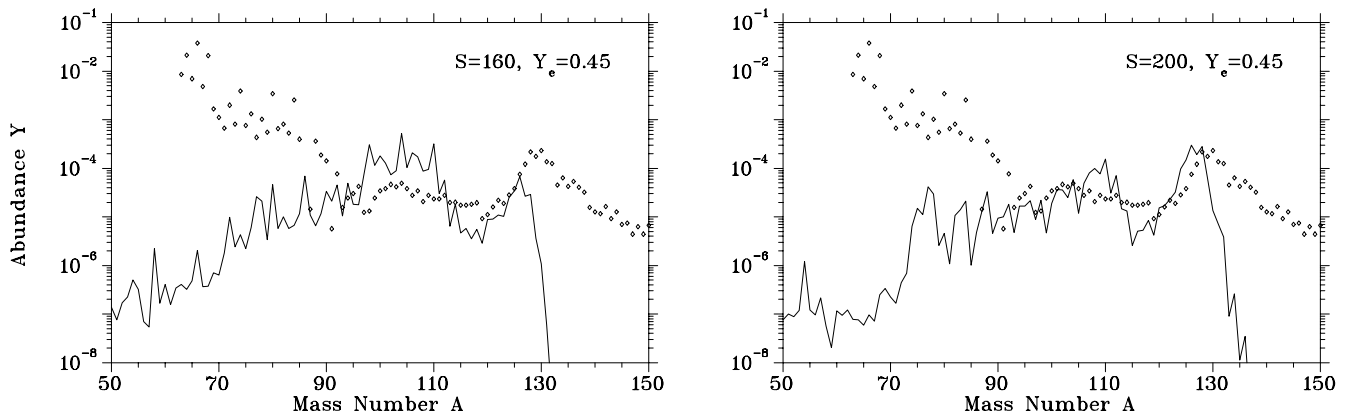


FIG. 7.—At entropies between  $S = 120$  and  $S = 220$  nuclei in the mass range  $90 < A < 130$  are most abundant. The  $A \approx 90$  peak of lower entropies is shifted up to  $A \approx 110$ . We see the onset of neutron captures and  $r$ -processing, producing the  $A \approx 130$  peak.

abundances from 90 to 110, but the amount of free neutrons is still negligible despite the rising  $X_\alpha$ . Only for  $S > 140$  does the remaining free-neutron fraction start to increase dramatically.  $X_\alpha$  starts to be the dominant mass fraction, and only free neutrons can compensate to attain the given global  $Y_e$  ( $=0.45$  in this discussion). This raises the  $Y_n/Y_{\text{seed}}$  ratio by several orders of magnitude up to  $Y_n/Y_{\text{seed}} \approx 30$  at  $S = 200$ . Thus, only when the entropies are approaching 200, the  $Y_n/Y_{\text{seed}}$  ratios of 30 start to permit *r*-process-type neutron captures up to the  $A = 130$  peak.

The most remarkable point here is the fact that the sequence of Figures 5–7 does not show a similarity to the solar system *r*-process abundance distribution in the appropriate mass range. In addition, odd-even effects are somewhat too large, which is, however, a problem of all *r*-process calculations at present. The abundance pattern is dominated by features from charged particle freezeout, and the  $Y_n/Y_{\text{seed}}$  ratios are too low for a subsequent *r*-process. Apparently the  $\alpha$ -rich freezeout seems not suitable to reproduce the solar pattern in the mass range  $80 < A < 110$  opposite to the pure neutron capture environment discussed in § 2, but this aspect will be discussed in more detail in § 4.

Raising the entropies from about 200 to about 350, the  $Y_n/Y_{\text{seed}}$  ratio grows from approximately 30 to 150. The  $\alpha$ -rich freezeout always produces seed nuclei in the range  $100 < A < 120$ , dependent on  $S$ . This material can then be “*r*-processed”, leading to a fully neutron-dominated process as discussed in § 2, and these components fit the solar *r*-process abundance pattern in the mass range  $A = 120$ –200 quite well (see Fig. 8). Thus, it is possible for this entropy range to establish a one-to-one correspondence between calculations based on entropies and expansion timescales ( $S$ ,  $\tau$ ) and the classical type of calculations, based on neutron separation energies of the *r*-path and timescales [ $S_n(n_n, T)$ ,  $\tau$ ], which were discussed in § 2. The neutron separation energy  $S_n$  of the *r*-process path is the one obtained during neutron capture freezeout in the entropy-based calculations [when also the  $(n, \gamma)$ – $(\gamma, n)$  equilibrium breaks down]. This correspondence can, however, only be established for entropies producing nuclei with  $A > 120$ . For none of the entropies discussed is an abundance peak at charged particle freezeout with  $A < 80$  obtained, leaving also a sufficient amount of neutrons for an *r*-process which would reproduce the typical neutron-induced abundance features in the range  $A = 80$ –110. Thus, this type of scenario

seems incapable of reproducing the solar *r*-process pattern for  $A < 110$ , unless a variation in  $Y_e$  would solve these problems.

### 3.4. Variations in $Y_e$

We have already seen that the entropy sequence for  $Y_e = 0.45$  produces *r*-process-like contributions to the mass range beyond  $A \approx 120$ , while for the smaller  $A$ -values some serious problems already became apparent. One might argue that this is just a bad choice in the parameter space ( $S$ ,  $Y_e$ ,  $\tau$ ), and that it might be possible to find parameter combinations that also fit the lower mass range. It is still another question whether the considered astrophysical scenario can provide such conditions.

In the following we want to examine how variations in  $Y_e$  change the overall properties of resulting abundances. The main effect is that lower  $Y_e$  values automatically increase the total neutron-to-nucleon ratio. Thus, for a given mass fraction of  $\alpha$ -particles remaining, the  $Y_{e,\text{heavy}}$  values will be smaller after the charged particle freezeout (depending on the choice of entropy), and thus more massive seed nuclei will be produced. In addition, the mass fraction of remaining free neutrons is larger. Therefore, the buildup of heavier nuclei is possible at lower entropies. We expect a scaling to lower entropies for lower  $Y_e$  values and vice versa for higher  $Y_e$  values due to the two effects (1) on  $Y_n/Y_{\text{seed}}$  and (2) on  $A_{\text{seed}}$ . We will have to investigate later whether this scaling can also influence the shape of the abundance patterns considerably. Figure 9 displays the  $Y_n/Y_{\text{seed}}$  ratio in the ( $S$ ,  $Y_e$ )-plane. A simple scaling with  $Y_e$  is clearly visible. This shows that smaller  $Y_e$  values would be one means to avoid the very high entropies required for the production of the *r*-process peak at  $A \approx 195$ .

Figures 10 and 11 show how  $Y_{\text{seed}}$  is dependent on  $Y_e$ , or better, what change in entropy is needed to obtain the same  $A_{\text{seed}}$  for different  $Y_e$  values. We see which ( $S$ ,  $Y_e$ ) combinations produce the peak at  $A \approx 90$ . For a high  $Y_e = 0.49$  an entropy of  $S = 110$  is necessary, whereas for  $Y_e = 0.35$  this peak is already produced at  $S = 30$ . This is another manifestation of the entropy scaling. Figures 10 and 11 seem also to indicate that in comparison to other elements the  $N = 50$  isotones are apparently always overproduced for any  $Y_e$ . This question will be addressed in more detail in § 4. If true, this makes it necessary to exclude a quite large region in the ( $Y_e$ ,  $S$ ) parameter-plane, in order to avoid the overproduction of the  $N \approx 50$  isotones and could be a chal-

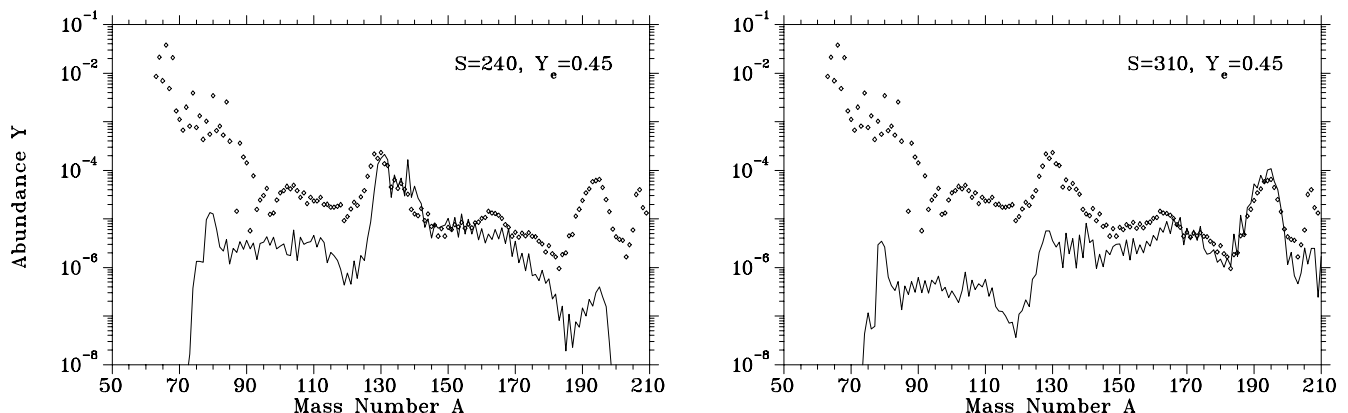


FIG. 8.—For  $S > 200$  the  $Y_n/Y_{\text{seed}}$ -ratio is high enough to cause a strong *r*-process. The good fit to the peak structures of the solar system *r*-process abundances is remarkable.

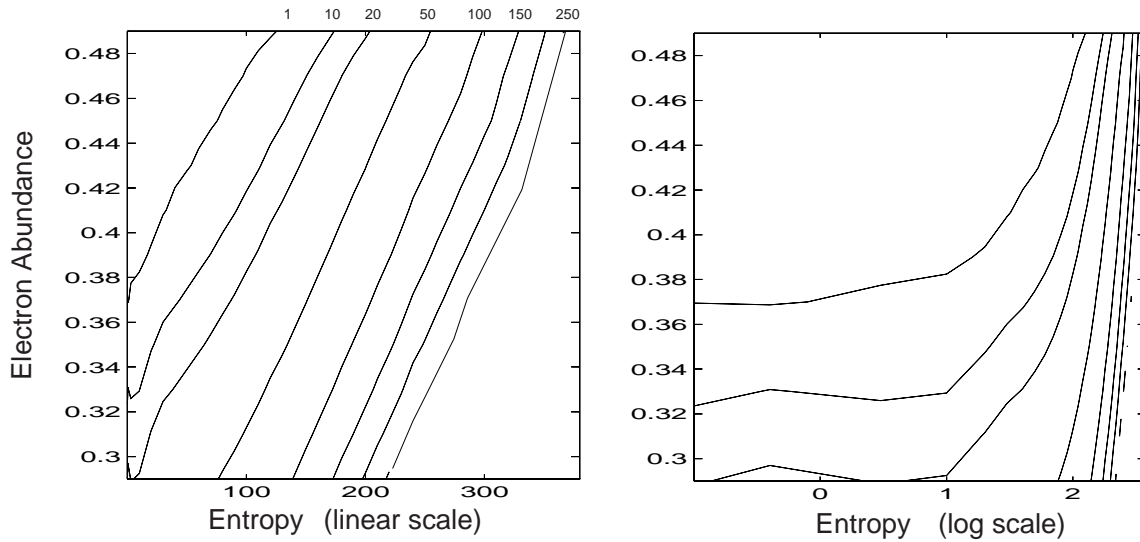


FIG. 9.— $Y_n/Y_{\text{seed}}$  in a contour plot as a function of initial entropy  $S$  and  $Y_e$  for an expansion timescale of 0.05 s as expected from SNe II conditions

length for the given astrophysical, high-entropy neutrino wind environment.

### 3.5. Variations in Expansion Timescales $\tau$

In our parameter study we used an expansion timescale of  $\tau = 50$  ms. This corresponds to an expansion velocity of

$4500 \text{ km s}^{-1}$  in our model. What effect do we expect due to variations of the timescale? For shorter timescales (faster expansion velocities), the most important effect to consider is the effect on the  $Y_n/Y_{\text{seed}}$  ratio, which determines the strength of the subsequent  $r$ -process. The shorter the timescale, the shorter the time for the  $\alpha$ -particles to recombine

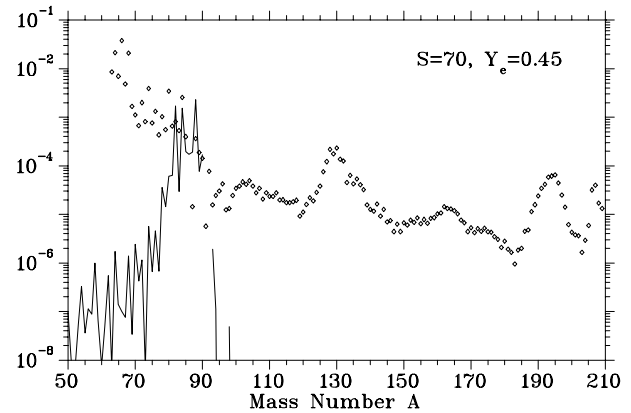
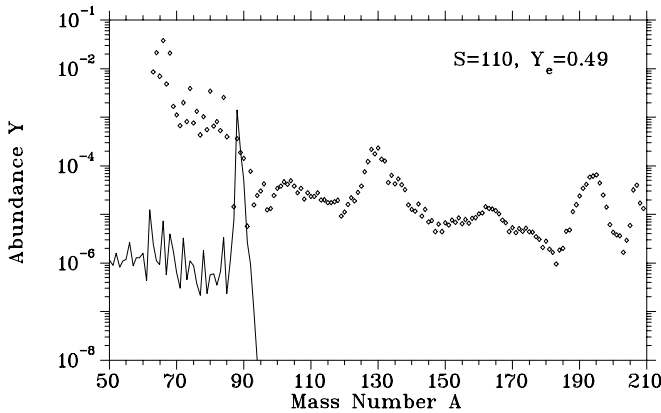


FIG. 10.—Illustration of the entropy scaling for abundance maxima after an  $\alpha$ -rich freezeout. For lower values of  $Y_e$  the  $A \approx 90$  peak is already synthesized at lower entropies. This region is always produced predominantly as a result of a charged-particle freezeout. But with decreasing  $Y_e$  the onset of small amounts of subsequent neutron processing can be observed.

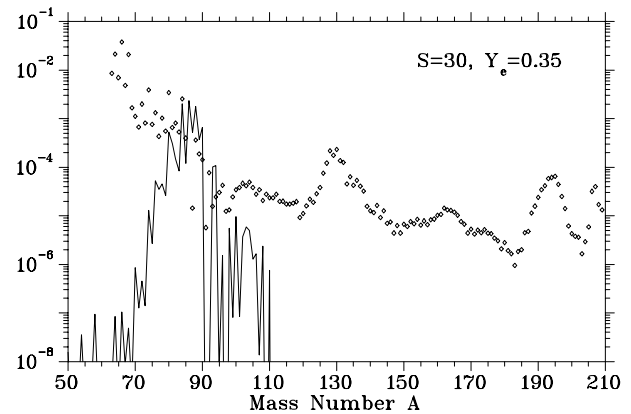
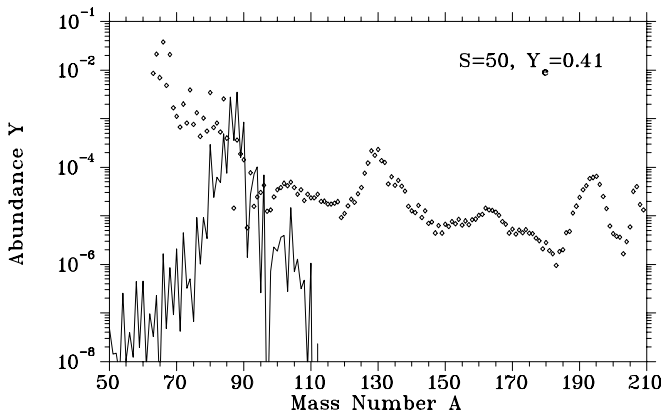


FIG. 11.—Sequence of Fig. 10 continued

through the  $3\alpha$  and  $\alpha\alpha n$  bottlenecks. Thus, the amount of heavy elements decreases, and the  $Y_n/Y_{\text{seed}}$  ratio is larger for the same entropy. In other words, for shorter timescales lower entropies are required for the synthesis of heavy elements. This is the second option to decrease the high entropy requirements and leads again to an entropy scaling (see also Hoffmann et al. 1997), but it does not cause significant changes in the corresponding abundance pattern.

Expansion timescales are clearly limited. With a time-scale of, e.g., 5 ms, equation (6) yields  $\dot{R} = 44,460 \text{ km s}^{-1}$ . This value is probably unrealistic. If one assumes a maximum expansion velocity of  $10,000 \text{ km s}^{-1}$  ( $\tau = 22 \text{ ms}$ ), the entropy required to produce the  $A = 195$  peak would decrease from  $S = 290\text{--}350$  to approximately the range  $S = 170\text{--}250$ , dependent on  $Y_e$ .

#### 4. A COMPARISON AND POSSIBLE CURES FOR ABUNDANCE DEFICIENCIES

After having presented the results of the site-independent, classical approach in § 2 and the entropy-based approach in § 3, we focus here on a comparison. This requires first the consideration of the structure of superpositions on an entropy grid. In line with the discussion in the Introduction (that observations ask for essentially one type of event to explain  $r$ -process abundances, at least above Ba), we made use of a smooth superposition of conditions as expected for different mass zones in a single astrophysical site. This is in agreement with the calculations of Wittl et al. (1994), who showed that the amount of mass ejected per entropy interval was relatively constant at late phases (when the higher entropy matter was expelled) and declining slightly at early phases (lower entropies) as a function of time (i.e., with increasing entropy). We follow these findings within a parameterized way, which allows us to optimize for the best possible fit to the solar abundance distribution. Together with presentation of the results of such superpositions we will give a comparison with § 2 and discuss possible similarities and differences of both approaches.

##### 4.1. Entropy Superpositions and Comparison to the Classical Approach

We choose the following *Ansatz* for the weighting function  $g(S_i)$ :

$$g(S_i) = x_1 e^{-x_2 S_i}, \quad i = 1, \dots, n, \quad (11)$$

with free parameters  $x_1$  and  $x_2$ , where the index  $i$  stands for individual entropy contributions. For each entropy the abundance pattern was obtained from calculations following equations (2)–(5) with the appropriate nucleosynthesis networks. This should be compared with equation (1) of the classical approach. The slope of  $g$  for  $S_i = 0$  is  $-x_1 x_2$  and  $g(S_i = 0) = x_1$ . Depending on the sign of  $x_2$  and its absolute value, the weighting function  $g(S_i)$  is increasing, constant, or decreasing with  $S$ . The two parameters are determined via a least-squares fit to the solar  $r$ -process abundances (measured) by minimizing the difference to a superposition of calculated abundance patterns:

$$\sum_A \left\{ \log Y_A^{\text{meas}} - \log \left[ \sum_{i=1}^n g(S_i) Y_A^{\text{calc}}(S_i) \right] \right\}^2. \quad (12)$$

This was done with the aid of multidimensional Newton-Raphson iterations. In order to test for variations in  $Y_e$ , we considered the superposition of contributions for two differ-

ent  $Y_e$  sequences (0.45 and 0.49). As our sample calculations showed already that the contributions producing  $A > 120$  had typical  $r$ -process features, while the lower entropy contributions for  $A \leq 120$  displayed a number of peculiarities, we first restricted our least-squares fit to the upper mass range.

For  $Y_e = 0.45$  the fit with the ETFSI mass formula resulted in  $x_1 = 797$  and  $x_2 = 2.63 \times 10^{-4}$ , which are typical values for all mass models. With this choice the weighting function is nearly flat (slightly decreasing for increasing entropy), in good agreement with the findings of Wittl et al. (1994). Similar results are obtained for the other mass formulae. In Figure 12 we therefore present the resulting  $r$ -process abundances for three different mass models, similar to Figure 3, with the same weighting function ( $x_1 = 1000$ ,  $x_2 = 0$ ), i.e.,  $g(S_i) = 1000 = \text{constant}$ . After the detailed analysis of one entropy sequence (§ 3.3) and the conclusion from § 3.4, we already expect that it will be hard to obtain a reasonable fit in the mass range  $80 < A < 120$ . Beyond  $A \simeq 110$  the corresponding mass models give fits of similar quality to those in Figure 3, and the discrepancies below the  $A \simeq 130$   $r$ -process peak, in the form of a pronounced trough, occur again for the FRDM and ETFSI mass models. Thus, our results and conclusions from § 2 can be translated also to the entropy-based approach for this mass region. The nuclear structure properties leading to agreement and deficiencies apply in the same way, due to the nature of a fast neutron freezeout, which preserves the abundances as they result from an initial  $(n, \gamma)$ – $(\gamma, n)$  equilibrium at high temperatures, even when neutron captures and photodisintegrations are followed explicitly.

Figure 13 shows the neutron number densities as a function of time for a range of entropies. Lower entropies ( $S \approx 200$ ) that contribute to the mass range  $A < 140$ , lead to an  $r$ -process with a fast (almost sudden) freezeout on short timescales of  $\tau \approx 0.04 \text{ s}$ . Thus, it is not surprising that the trough before  $A \simeq 130$ , due to shell structure far from stability and its effect on abundance patterns in an  $(n, \gamma)$ – $(\gamma, n)$  equilibrium, survives.

There is possibly one difference from the conclusions given with Figure 3. As can be seen from Figure 13, the calculations experiencing the highest entropies show the longest neutron freezeout timescales. On the other hand, they are responsible for the heaviest nuclei with the largest neutron capture cross sections. Our results show that the trough before the  $A \simeq 195$  peak, resulting in the case of the ETFSI mass model and a waiting-point approach (Thielemann et al. 1994; Chen et al. 1995; Bouquellé et al. 1996; Pfeiffer, Kratz, & Thielemann 1997), does not survive. This  $r$ -process abundance region is changed by ongoing (nonequilibrium) neutron captures during the freezeout and does not directly witness nuclear properties far from stability at the  $N = 126$  shell closure. In Figure 12 we actually observe a filling of the minimum before the  $A \simeq 195$  peak, and even the ETFSI masses, which produced the largest trough in the waiting-point calculations of Thielemann et al. (1994) and Chen et al. (1995), seem to give a good fit.

However, this conclusion is strongly based on the neutron capture cross sections far from stability, which enter during the nonequilibrium phase after freezeout. Possible changes of giant dipole characteristics, due to a large neutron skin of such neutron-rich nuclei, can enhance the dominant E1  $\gamma$ -transitions at low energies for such reactions with small neutron capture  $Q$ -values. Recent studies by

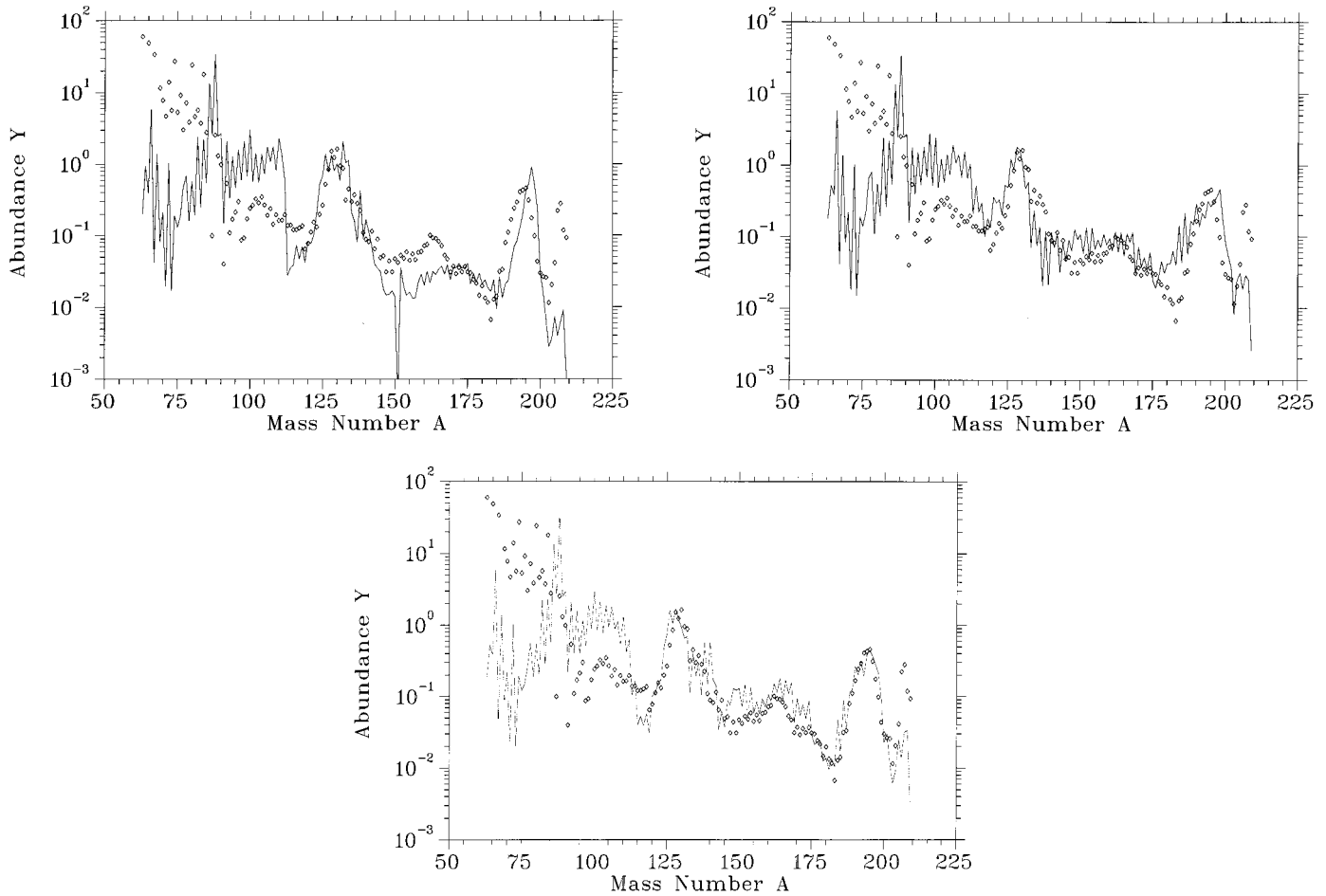


FIG. 12.—Similar to Fig. 3 with the FRDM (Möller et al. 1995), droplet model (Hilf, von Groote, & Takahashi 1976), and ETFSI (Aboussir et al. 1995) mass formulae, making use of a superposition of entropies according to equation (11) which simulates  $r$ -process conditions from the high-entropy neutrino wind in SNe II. This calculation was performed with  $Y_e = 0.45$ , but similar results are obtained in the range 0.30–0.49, only requiring a scaling of entropy. The trough below  $A = 130$  behaves similarly to that in Fig. 3, the smoother (although not perfect) behavior of the Hilf masses (Hilf et al. 1976) avoids this gap. This shows that every time-dependent freezeout (with a full treatment of neutron captures and photodisintegrations) resulting from a more realistic astrophysical scenario can cause the same abundance deficiencies due to specific nuclear structure features as obtained in an instantaneous freezeout from an  $(n, \gamma)$ – $(\gamma, n)$  equilibrium in classical site-independent calculations. The trough before the  $A \approx 190$  peak, existing, e.g., for the ETFSI mass formula in the waiting-point approximation and an instantaneous freezeout, is filled because of neutron freezeout effects. The strong deficiencies in the abundance pattern below  $A \approx 110$  are due to the  $\alpha$ -rich freezeout and are thus mainly related to the astrophysical scenario rather than to nuclear structure.

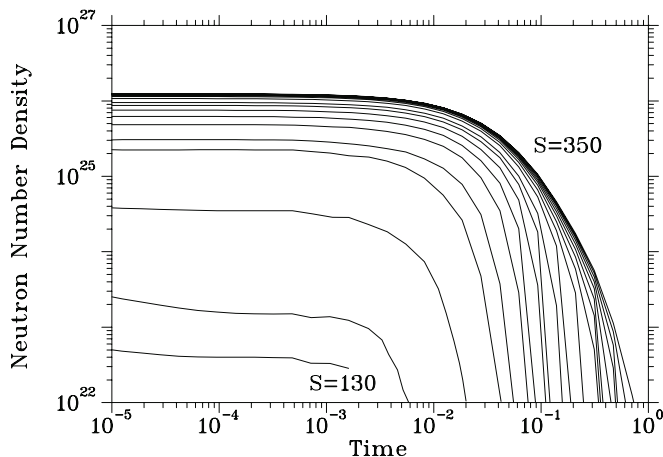


FIG. 13.—Value  $n_n$  as a function of time, displayed for different entropies  $S = 130, 140, \dots, 350$ .

Goriely (1998) show that this could increase cross sections by up to a factor of 100. As the same applies to the reverse photodisintegrations (detailed balance), consequently an  $(n, \gamma)$ – $(\gamma, n)$  equilibrium could hold much longer. That could change the features of Figure 12 below the  $A \approx 195$  peak back to those of Figure 3, and even in an entropy-based approach this second nuclear structure signature (in addition to the trough below  $A \approx 130$ ) would be visible.

A different important aspect can be noticed from Figure 13, with respect to the timescales required to produce the heaviest nuclei. They are in all cases less than 1 s, different from § 2 with constant  $n_n$  and  $T$ , where durations up to 2.5 s were needed. This is due to the fact that the site-independent, classical studies of § 2 make use of the same  $r$ -process paths throughout the calculation, which also give the final imprint on abundance features. In the present entropy studies, the  $r$ -process path of a given entropy component is initially closer to the neutron drip line (experiencing shorter  $\beta$ -decay half-lives), and only the path at neutron freezeout coincides with the one from the studies

in § 2. This would also mean that an enhancement of “effective”  $\beta$ -decay rates via neutrino captures [ $\nu + (Z, A) \rightarrow (Z + 1, A) + e^-$ ] as discussed in Qian, Vogel, & Wasserburg (1998) would not necessarily be required.

The same procedure as discussed above for  $Y_e = 0.45$  was followed for a superposition of components with  $Y_e = 0.49$  (see Fig. 14). Besides differences in detail, it is remarkable that the results for  $A > 110$  look very similar to the ones discussed for  $Y_e = 0.45$ . The  $A = 130$ – $200$  region is fitted reasonably well with similar agreements and deficiencies for the same mass models. The trough below  $A = 195$  is also filled for the ETFSI mass model due to a slow freezeout of neutron captures. The trough before  $A = 130$  remains for both mass models FRDM and ETFSI. However, in order to obtain the same full abundance pattern, higher entropies are needed for a  $Y_e$  of 0.49. While the  $A = 195$  peak can be reproduced with  $S = 290$  for  $Y_e = 0.45$ ,  $S = 340$  is required for  $Y_e = 0.49$ . This relates to a changing behavior of the  $\alpha$ -rich freezeout with  $Y_e$  as discussed in § 3.3. It also requires a different superposition law, which is found for all three mass models to increase with entropy, according to  $x_1 = 1000$  and  $x_2 = 6 \times 10^{-3}$ , i.e.,  $g(S_i) = 1000 \exp(6 \times 10^{-3} S_i)$ . This results in a weight at  $S = 350$  being higher by a factor of 8 than the weight at  $S = 0$ . Such behavior is necessary because at  $Y_e = 0.49$ , higher entropies are required for

the production of the high mass contributions that lead to a stronger  $\alpha$ -rich freezeout. This produces less seed nuclei for the highest entropy components, responsible for the larger mass numbers, and thus requires the weighting function to increase with increasing entropy to compensate for this effect.

Let us finally turn to the abundances in the range  $A < 110$ . It is visible in Figure 12 that this mass range has a very different behavior from that in Figure 3. As discussed above, within a high-entropy environment this mass region is not produced via neutron captures, but results from the neutron-deficient  $\alpha$ -rich freezeout for lower (high) entropies (still sufficiently high to cause an  $\alpha$ -rich freezeout). It is remarkable that every superposition results in a large overabundance in the range  $90 < A < 110$ . Hoffman et al. (1996) reported that the overproduction of  $N = 50$  isotones ( $A \approx 85$ – $90$ ) is cured as soon as  $Y_e$  becomes larger than approximately 0.485. We see this also to a certain extent. The very strong spike around  $A \approx 90$  is reduced when changing  $Y_e$  from 0.45 to 0.49. This can be understood within the framework discussed in § 3.3. The  $N = 50$  isotones are the result of an  $\alpha$ -rich freezeout for  $Y_{e,\text{heavy}}$  in the range 0.466–0.410. For  $Y_{e,\text{global}} = 0.45$  this  $Y_{e,\text{heavy}}$  range (being close to but smaller than  $Y_{e,\text{global}}$ ) is experienced for a large fraction of the lower entropies. Thus, the  $N = 50$  iso-

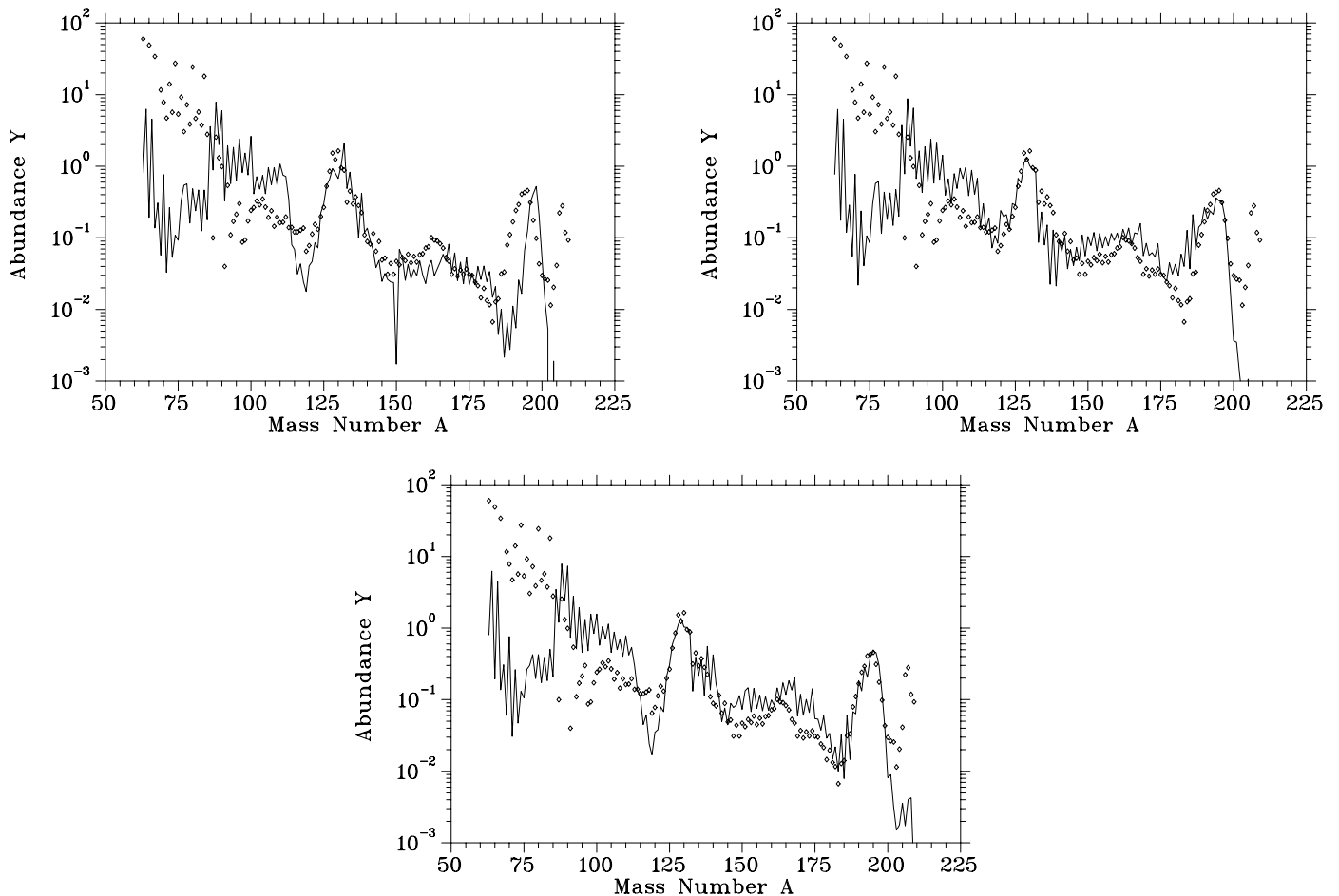


FIG. 14.—Superposition for  $Y_e = 0.49$  and the same mass models as in Fig. 12. The abundances for  $A > 110$  are similar to the results for  $Y_e = 0.45$ . The range  $90 < A < 110$  shows a slightly different behavior, as the  $A = 90$  peak ( $N = 50$ ) is not so pronounced, due to the fact that  $Y_{e,\text{heavy}} > 0.446$  lines do have intersections in the nuclear chart with  $\alpha$  separation energies of  $\approx 6$  MeV already for  $N < 50$ . The  $A < 110$  mass range is in total still overproduced, and only a reduced weighting of lower entropies can cure this. Neither case can account for the  $A \approx 80$  *r*-process peak.

tones are accompanied by a strong weight. For  $Y_e = 0.49$  the lower entropies populate nuclei at similar  $\alpha$  separation energies of  $\approx 6$  MeV in the  $\alpha$ -rich freezeout, but for  $Y_{e,\text{heavy}} \approx Y_{e,\text{global}} > 0.446$ . These are nuclei in the valley of stability or even on its proton-rich side for  $N < 50$  (see Fig. 13 in Möller et al. 1997) and contours of  $Q_\alpha = -6$  MeV). Once  $Y_{e,\text{heavy}}$  becomes smaller than  $Y_{e,\text{global}}$  (see eq. [8]), due to the increasing strength of the  $\alpha$ -rich freezeout with entropy, it changes fast as a function of entropy. Consequently, there is not a strong weight in components with  $Y_{e,\text{heavy}} = 0.446\text{--}0.410$ , which produce  $N = 50$  isotones.

Independent of the  $N = 50$  abundance features, for  $Y_e = 0.45$  as well as  $0.49$  a strong overproduction is found for the whole region  $90 < A < 110$ , which is also due to a neutron-poor but  $\alpha$ -rich freezeout. It looks less severe for the  $Y_e = 0.49$  case, owing to the absence of the spike at  $N = 50$  and a decreasing weight function with decreasing entropy. It is not obvious what weight such mass zones would carry in a realistic astrophysical environment, but in order to be compatible with solar  $r$ -abundances a much smaller weight would be needed for the lower entropies than equation (11) predicts with the best-fit choice for  $x_1$  and  $x_2$ .

A mass region that is not produced in either of the cases is the first and important  $A \approx 80$   $r$ -process peak, showing underabundances by a factor of the order of 100. This region can only be well reproduced (see § 2 and Fig. 3) but nuclei with neutron separation energies of the order  $S_n \approx 3.8$  MeV in the vicinity of the  $N = 50$  closed shell and not by any neutron-poor  $\alpha$ -rich freezeout. Figure 2b in Hoffman et al. (1996) shows the same effect if one considers that ratios in comparison with solar abundances and not with solar  $r$ -abundances are shown. The  $r$ -process nuclei in that plot are the neutron-rich isotopes, which are underabundant by about a factor of 100.

In total, the results of high-entropy superpositions discussed in this subsection can be characterized by two aspects in comparison with the classical approach: (1) for  $A > 110$  both approaches lead to very similar  $r$ -process patterns, and nuclear structure features show up in a very similar way. Thus, we have a sound basis to relate  $r$ -process patterns and deficiencies to nuclear structure. (2) For  $A < 110$  high-entropy environments are dominated by abundance patterns that relate to  $\alpha$  separation energies and not to neutron separation energies. Such behavior is not

comparable to the classical approach and also does not agree with solar  $r$ -abundances in this mass region. There are several possible conclusions to be drawn from this: (1) the high-entropy wind is not the correct  $r$ -process site (due to inherent deficiencies in the abundance pattern below  $A \approx 110$  as well as the problems in obtaining the high entropies in SN explosions, required for producing the massive  $r$ -process nuclei with  $A \approx 195$ ), or (2) the high-entropy wind model overcomes the problems in attaining sufficiently high entropies and produces the masses beyond  $A \approx 110$ , but avoids or dilutes strongly the ejection of the lower entropy matter. In the latter case another site has to be responsible for the lower mass region.

#### 4.2. Low- $Y_e$ , Low-Entropy Environments

In order to obtain a good reproduction of  $r$ -process abundances for  $A < 110$ , a higher neutron density is required for lower entropies, which leads to an abundance pattern being also dominated by neutron separation energies for nuclei with  $A < 110$ . An extension of  $Y_e$  to smaller values, as low as 0.3, could in itself solve the problem. This might be possible by constraining  $v_e$  and  $\bar{v}_e$  fluxes and mean energies in supernova environments (Qian & Woosley 1996). But in addition to a lower  $Y_e$ , also lower entropies are required. This can be deduced from Figure 9b. It shows the  $Y_n/Y_{\text{seed}}$  ratio plotted in the  $(S, Y_e)$ -plane with a logarithmic entropy axis extending to down entropies as low as  $S = 10^{-2}$ . Here the simple linear scaling with  $S$  is no longer valid. The contour lines form a plateau and depend only on  $Y_e$ . This can be interpreted in the way that entropies below  $0.15 k_B \text{ baryon}^{-1}$  (see § 3.1) lead to a normal rather than an  $\alpha$ -rich freezeout. In such a case (lacking  $\alpha$ -particles) we have  $Y_{e,\text{heavy}} = Y_{e,\text{global}}$ , and  $Y_n/Y_{\text{seed}}$  is only determined by  $Y_e$  (independent of the entropy). A normal (but not  $\alpha$ -rich) freezeout causes an abundance distribution of heavy nuclei after charged particle freezeout around  $A \approx 50\text{--}70$  (not being tilted to larger  $A$ -values by large remaining  $\alpha$  fractions). The amount of neutrons left is large enough to produce the abundance pattern in the range  $80 < A < 130$  in a clearly neutron capture-dominated process, which results in a similarly good fit (see Fig. 15) to those obtained in site-independent, classical studies based on neutron densities rather than entropies (see Fig. 1). In order to cover the whole range of  $Y_n/Y_{\text{seed}}$  ratios for reproducing a full  $r$ -

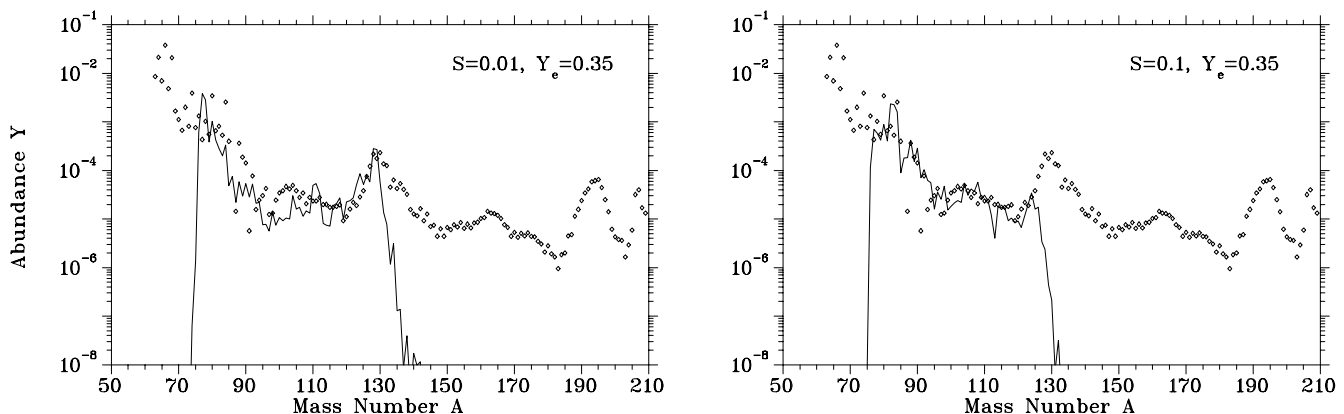


FIG. 15.—A low  $Y_e = 0.35$  value and a high density  $\rho > 10^7 \text{ g cm}^{-3}$  ensure a normal (low-entropy) freezeout with a sufficient amount of neutron left for the synthesis of  $80 < A < 120$  nuclei. This calculation utilizes the droplet model by (Hilf et al. 1976) and thus avoids the trough for  $110 < A < 120$ . A further decrease in  $Y_e$  (see Fig. 9b) will increase the  $Y_n/Y_{\text{seed}}$  ratio to account also for the upper mass range of  $r$ -process nuclei. Such an environment is similar to the traditionally discussed low- $Y_e$  and high-density scenarios related to neutron stars (see, e.g., Cowan et al. 1991; Meyer 1994).

process abundance pattern,  $Y_e$  has to extend down to 0.13 in normal freezeout (low-entropy) conditions. It has been shown before (Meyer 1989; Hillebrandt, Takahashi, & Kodoma 1976) that for such sufficiently  $Y_e$  values (cold decompression of neutron star matter) the upper end of the  $r$ -process can be produced as well.

#### 4.3. Possible Effect of Neutrinos

There have been suggestions that neutrino-induced spallation of nuclei in the  $A \simeq 130$  and 195 peaks, caused by a strong neutrino wind from the hot neutron star, can play an important role (Qian et al. 1996). We performed cross section calculations for these neutrino-induced processes, which are given in Table 2 for a typical nucleus in this mass region and based on the continuum RPA calculations discussed elsewhere (Kolbe et al. 1992). These are only the neutral current cross sections. Charged current reactions, like ( $\nu_e, e^-$ ), can produce nuclei at similar excitation energies (due to the same  $\nu_e$  spectrum) and thus also lead to neutrino spallation. The rates for both types of reactions are of the same order (Qian et al. 1996) for the same neutrino energies. Multiplying these cross sections  $\sigma_\nu(T, \mu)$  (already averaged over a neutrino distribution and characterized by temperature  $T$  and a chemical potential  $\mu$ ) with a neutrino flux  $\Phi_\nu$  gives the reaction rates  $\lambda_\nu = \sigma_\nu \Phi_\nu$ . The neutrino flux  $\Phi_\nu(t)$ , experienced by a mass zone at a radius  $r(t)$  at time  $t$  is given by (Fuller & Meyer 1995; Qian et al. 1996)

$$\Phi_\nu(t) = 4.97 \times 10^{41} \left( \frac{L_\nu(t)}{10^{51} \text{ ergs s}^{-1}} \right) \left( \frac{\text{MeV}}{\langle E_\nu \rangle} \right) \times \left( \frac{100 \text{ km}}{r(t)} \right)^2 \text{ cm}^{-2} \text{ s}^{-1}, \quad (13)$$

where  $L_\nu(t)$  is the total neutrino luminosity of the cooling neutron star at time  $t$  and  $\langle E_\nu \rangle$  the average neutrino energy. While ( $\nu_e, e^-$ ) can be of importance for the whole duration of the  $r$ -process, behaving like a  $\beta^-$  decay from  $Z$  to  $Z + 1$  and thus causing effectively an acceleration of the  $r$ -process (Qian et al. 1998),  $\nu$ -spallation, producing nucleus ( $A - i$ ) plus  $i$  neutrons is only of importance during the final neutron freezeout. Only then neutron captures and photo-disintegrations will not immediately “repair” the damage and move back to ( $n, \gamma$ )-( $\gamma, n$ ) equilibrium abundances. This neutral current, neutrino-induced spallation can also be caused by  $\mu$  and  $\tau$  neutrinos, which have higher average energies than electron neutrinos ( $\langle E_{\nu_{\mu,\tau}} \rangle \approx 25 \text{ MeV} = \pi T_{\nu_{\mu,\tau}}$  with a temperature of the order of 8 MeV). At the time of the freezeout, when this effect could be of importance, matter has moved to a distance of 1000 km from the neutron star in the original calculations by Woosley et al.

(1994). Making use of equation (13) for  $\Phi_\nu(t)$  with  $r = 1000$  km,  $L_{\nu,0} = 5 \times 10^{50}$  ergs  $\text{s}^{-1}$  and a decline of  $L_\nu(t = 1000 \text{ s})/L_{\nu,0} = 0.318$  (from the original calculations by Woosley et al. 1994), results for  $T_{\nu_{\mu,\tau}} = 8$  MeV in  $\lambda_\nu = \sigma_\nu (T_{\nu_{\mu,\tau}} = 8 \text{ MeV}, \mu = 0) \Phi_{\nu_{\mu,\tau}}(1000 \text{ s}) = 3.5 \times 10^{-5} \text{ s}^{-1}$  or a neutrino spallation half-life (if taking into account four flavors) of  $\tau_\nu = \ln 2/\lambda_\nu = 5 \times 10^3$  s, after which 50% of the nuclei are destroyed by this effect. If one includes the information that such a mass zone moves out to larger radii (and each factor of 10 leads to a decrease in the flux by a factor of 100), the effect of neutrino spallation seems marginal. This framework can only be changed by also changing  $L_\nu$ , and especially  $r(t)$  to be of the order of several 100 km (Qian et al. 1998).

Here we would like to discuss whether this effect could cause a filling of the abundance troughs below the  $A \sim 130$  (and 195) peaks, which resulted in the classical as well as entropy-based calculations for mass models without shell quenching far from stability. The abundance trough below the 130 peak has to be filled down to  $A \approx 110$  with about 5% of the peak abundance at  $A \simeq 130$  in order to obtain the solar  $r$ -abundance pattern. If only one neutron is emitted in each spallation event, it requires 20 events to produce the  $A \simeq 110$  abundance from  $A \simeq 130$  nuclei, and each nucleus has to have undergone  $\nu$ -spallation with an efficiency of 86% ( $0.86^{20} = 0.05$ ). If we assume as an absolute upper limit four emitted neutrons, only five events have to occur, leading to a required efficiency of 55% ( $0.55^5 = 0.05$ ). In both cases we would expect not only a filling of the trough but also an unwanted change of the peak abundance pattern.

Thus, while abundance effects of order 1 are possible by neutrino spallation in the wings of the  $A = 130$  peak (down to  $A = 124$ ; Qian et al. 1996), and maybe this effect could improve the too-large odd-even staggering in abundances, we still need for the large trough in the mass region  $110 < A < 120$  the nuclear structure effects (shell quenching far from stability) outlined in detail in Chen et al. (1995) and Kratz, Pfeiffer, & Thielemann (1998) as well as in §§ 2 and 4.1, especially as such effects are already observed experimentally. For a general review of whether neutrino interactions with matter actually support or hinder the occurrence of an  $r$ -process, when taken into account in a consistent way for nucleons and light as well as heavy nuclei, see Meyer, McLaughlin, & Fuller (1998).

## 5. SUMMARY AND OUTLOOK

In the present paper we followed the expansion of matter with initial high entropies  $S$  (as expected from a high-entropy neutrino wind in supernovae) on expansion time-scales  $\tau$  through the freezeout of reactions with declining

TABLE 2

TOTAL INTEGRATION CROSS SECTIONS FOR NEUTRAL CURRENT NEUTRINO SCATTERING<sup>a</sup>

$(T, \alpha)$	(4, 0)	(6, 0)	(8, 0)	(10, 0)	(3, 5)	(5, 5)
$^{130}\text{Cd}(\nu, \nu'p)^{129}\text{Ag}$ .....	2.1 (-8)	1.5 (-6)	1.2 (-4)	1.2 (-4)	5.7 (-10)	2.2 (-7)
$^{130}\text{Cd}(\nu, \nu'n)^{129}\text{Cd}$ .....	9.1 (-2)	3.8 (-1)	1.1 (0)	2.4 (0)	2.8 (-2)	1.8 (-1)
$^{130}\text{Cd}(\nu, \nu'\alpha)^{126}\text{Pd}$ .....	1.5 (-7)	1.7 (-5)	1.6 (-3)	1.6 (-3)	2.8 (-9)	2.1 (-6)
Total.....	9.1 (-2)	3.8 (-1)	1.1 (0)	2.4 (0)	2.8 (-2)	1.8 (-1)

<sup>a</sup> The cross sections are given per nucleon in units of  $10^{-42} \text{ cm}^2$  and averaged over neutrinos and antineutrinos.

temperatures and densities. While this has been done before by a number of investigators, this is the first time that different nuclear mass models have been explored in such dynamic investigations. We compared the similarities and differences between this approach and the classical, site-independent approach, based on (constant) neutron number densities  $n_n$ , temperatures  $T$ , duration times  $\tau$ , and the assumption of an  $(n, \gamma)$ – $(\gamma, n)$  equilibrium (Kratz et al. 1998, 1993). We examined especially whether there exists a one-to-one mapping between the two approaches:

1. We could show that this is the case for entropies that lead to a strong  $\alpha$ -rich freezeout of charged particle reactions with a large final neutron-to-seed ratio. In these cases the charged particle reactions are followed by an  $r$ -process with very high neutron number densities, which ensure an  $(n, \gamma)$ – $(\gamma, n)$  equilibrium, produce nuclei with mass numbers  $A > 110$  in similar quantities in comparison to solar, and the neutron separation energy of the  $r$ -path at neutron freezeout is the same one as in the corresponding components of the classical approach with constant  $n_n$  and  $T$ .

a) Concerning the influence of nuclear properties far from stability, we could show that the conclusions of the classical, site-independent calculations of Kratz et al. (1993), Chen et al. (1995), and Pfeiffer et al. (1997) remain valid for the  $A \simeq 130$  region. All contributions to this mass region are synthesized for conditions with short freezeout timescales that are well described by the waiting-point approximation with a sudden freezeout. For both approaches the abundance deficiencies can be cured by quenching of shell effects from stability.

b) For the  $A \simeq 195$  peak this is not so evident. The freezeout timescales of the corresponding components are long, and nonequilibrium neutron captures can fill the trough before the peak. This can result in a good fit even for the ETFSI mass model, which led to the most pronounced trough in previous calculations within the waiting-point approximation. Thus, the one-to-one mapping for the two approaches might not be fully correct, as the freezeout can cause moderate changes for the high-entropy components that produce nuclei with  $A > 150$ –160. A recently discussed enhancement of neutron-capture rates, due to changes in giant dipole resonance properties of neutron-rich nuclei with neutron skins, could, however, potentially change matters again toward a one-to-one mapping, as  $(n, \gamma)$ – $(\gamma, n)$  equilibria, which caused the troughs in the classical approach, are attained for a longer period.

2. There exists no correspondence between the classical and the entropy-based approach for lower (high) entropy contributions (in our model  $S = 200$  and below for  $Y_e = 0.45$ ). Under these conditions the neutron number densities  $n_n$  after charged particle freezeout are marginal and have no influence on the related abundance pattern, which covers the mass range  $80 < A < 110$  and is the produce of charged particle reactions and a neutron-poor,  $\alpha$ -rich freezeout. It is not meaningful to compare these contributions to classical  $r$ -process calculations.

a) Our detailed analysis shows also that it is not possible to obtain a good fit for these components to the solar system  $r$ -process abundance pattern in the mass range  $A < 110$ , unless a nonmonotonous weighting of components with lower entropies is used. The first  $r$ -process peak at  $A = 80$  is impossible to reproduce in such an environment. Instead of a peak at  $A \simeq 80$ , a strong overproduction of  $A \simeq 90$ –110 nuclei (somewhat dependent on

the mass model and  $Y_e$ ) occurs. To avoid the overproduction of these elements, it is necessary to exclude quite large region in the  $(Y_e, S)$ -parameter plane at lower entropies.

b) We could show, however, that conditions with low entropies  $S < 0.1$  and low  $Y_e$  values of the order of 0.35, which lead to a normal (i.e., not  $\alpha$ -rich) freezeout and subsequent neutron captures, can provide neutron densities that resemble the classical  $r$ -process discussed already in the site-independent classical studies of § 2. They can produce a good fit to the solar abundance pattern in the mass range  $80 < A < 130$  (Figs. 15 and 9) and might correspond to astrophysical sources related to expanding neutron star matter.

3. What can we learn from these entropy-based studies and the fact that the  $r$ -process abundances below  $A = 110$  cannot be reproduced correctly for high-entropy environments? There exist several possible conclusions:

a) The high-entropy wind is not the correct  $r$ -process site, owing to the inherent deficiencies in the abundance pattern below  $A = 110$ , as well as the problems in obtaining the high entropies in SNe II explosions, required for producing the massive  $r$ -process nuclei up to  $A \simeq 195$  and beyond.

b) The high-entropy wind scenario in supernovae overcomes the problems in attaining such high entropies and produces only the masses beyond  $A = 110$ , avoiding or diluting the ejection of the lower entropy matter. In the latter case another site has to be responsible for the lower mass region.

c) Such a site has to be characterized by  $Y_e$  values as small as 0.3, and also lower entropies close to a normal freezeout ( $S \sim 1$ ). Cold high-density matter in  $\beta$  equilibrium (see Meyer 1989; Hillebrandt, Takahashi, & Kodoma 1976) would fulfill these constraints. Variations in  $Y_e$  down to 0.13 would also provide  $Y_n/Y_{\text{seed}}$  ratios sufficient to produce heavy  $r$ -process nuclei.

d) Whether such an interpretation ( $A < 130$  from low- $Y_e$  and low- $S$  conditions,  $A > 130$  from high- $S$  conditions) is the solution, or low- $S$  conditions also produced heavy  $r$ -process nuclei, might eventually be answered by observations. There seems to exist meteoritic evidence, discussed by Wasserburg, Busso, & Gallino (1996), that the last  $r$ -process contributions to the solar system for  $A > 130$  and  $A < 130$  came at different times, i.e., from different types of events deduced from the extinct radioactivities  $^{107}\text{Pd}$ ,  $^{129}\text{I}$ , and  $^{182}\text{Hf}$  in meteoritic matter. It is highly desirable to have an independent verification of this from observations of low-metallicity stars, which apparently show a completely solar  $r$ -process composition for nuclei with  $A > 130$  (Snedden et al. 1996; Cowan et al. 1997), possibly stemming from the first events in our Galaxy that produce  $r$ -process nuclei (Mathews, Bazan, & Cowan 1992). It is also necessary to explore the abundances of nuclei with  $A < 130$  in such observations, in order to test whether the solar pattern will also be found there or is absent, owing to different evolution timescales of two independent stellar sources for these different mass ranges of  $r$ -process nuclei.

The results presented in this study benefitted from discussions with A. Burrows, W. Hillebrandt, R. Hoffman, P. Vogel, H.-T. Janka, Y.-Z. Qian, and the referee S. E.

Woosley. This work was supported by the Swiss Nationalfonds (grants 20-47252.96 and 20-053798.98), the German BMBF (grant 06Mz864) and DFG (grant Kr806/5), the US

NSF (grants AST 9618332 and PHY 9407194), the DOE (contract DE-AC05-96OR22464), and the Austrian Academy of Sciences.

## APPENDIX A

### DYNAMIC *r*-PROCESS CALCULATIONS

This study was performed with a full dynamic *r*-process code, utilizing the numerical techniques published in Cowan et al. (1991) and Cowan, Cameron, & Truran (1983). This scheme linearizes the set of differential equations for the individual abundance evolutions by assuming a slow change of  $Y_n$ , approximated to be constant during each time step.  $Y_n$  is evolved via mass conservation. Therefore, mass conservation is no longer an independent quantity that can be used to control the accuracy of the calculation. We have to require

$$\left| \frac{\Delta Y_n}{Y_n} \right| \ll 1 \quad (\text{A1})$$

for each time step in order to apply this approximation. A simple formula for a rough estimate of the above condition can be related to the  $X_n/X_{\text{seed}}$  ratio, where  $X_{\text{seed}}$  is the mass fraction of all nuclei that capture neutrons. The change of  $Y_n$  over each time step is given by mass conservation,

$$\Delta Y_n = -\sum_{i,j} A_j \Delta Y_{(Z_i, A_j)}. \quad (\text{A2})$$

The  $X_n/X_{\text{seed}}$  ratio can be written in the form

$$\frac{X_n}{X_{\text{seed}}} = \frac{X_n}{\sum_{i,j} A_j Y_{(Z_i, A_j)}} = r; \quad (\text{A3})$$

$X_n$  can be replaced by  $Y_n$  due to  $X_n = A_n Y_n = Y_n$ . When choosing time steps that ensure that typical abundance changes are not larger than the fraction  $f$  ( $|\Delta Y_{(Z_i, A_j)}| \leq f Y_{(Z_i, A_j)}$ ), equation (A3) can be expressed in the following way:

$$|Y_n| = r \sum_{i,j} A_j Y_{(Z_i, A_j)} \geq \frac{r}{f} \sum_{i,j} A_j |\Delta Y_{(Z_i, A_j)}| \geq \frac{r}{f} \left| \sum_{i,j} A_j \Delta Y_{(Z_i, A_j)} \right| = \frac{r}{f} |\Delta Y_n|, \quad (\text{A4})$$

or

$$\left| \frac{\Delta Y_n}{Y_n} \right| \leq \frac{f}{r}. \quad (\text{A5})$$

Thus, the fractional abundance change  $f$  has to be chosen according to the neutron/seed ratio  $r$  in order to attain a sufficiently small  $\Delta Y_n/Y_n$  and ensure the validity of the linear approximation.

### REFERENCES

- Aboussir, Y., Pearson, J. M., Dutta, A. K., & Tondeur, F. 1995, *At. Data Nucl. Data Tables*, 61, 127
- Bao, Z. Y., & Käppeler, F. 1987, *At. Data Nucl. Data Tables*, 36, 411
- Blake, J. B., Woosley, S. E., Weaver, T. A., & Schramm, D. N. 1981, *ApJ*, 248, 315
- Bouquelle, V., Cerf, N., Arnould, M., Tachibana, M., & Goriely, S. 1996, *A&A*, 305, 1005
- Cameron, A. G. W., Cowan, J., & Truran, J. W. 1983, *Ap&SS*, 91, 235
- Campi, X., Flocard, H., Kerman, A. K., & Koonin, S. 1975, *Nucl. Phys. A*, 251, 193
- Caughlan, G. R., & Fowler, W. A. 1988, *At. Data Nucl. Data Tables*, 40, 283
- Chen, B., Dobaczewski, J., Kratz, K.-L., Langanke, K., Pfeiffer, B., Thielemann, F.-K., & Vogel, P. 1995, *Phys. Lett. B*, 355, 37
- Cowan, J. J., Cameron, A. G. W., & Truran, J. W. 1983, *ApJ*, 265, 429
- . 1985, *ApJ*, 294, 656
- Cowan, J. J., McWilliam, A., Sneden, C., & Burris, D. L. 1997, *ApJ*, 480, 246
- Cowan, J. J., Thielemann, F.-K., & Truran, J. W. 1991, *Phys. Rep.*, 208, 267
- Dobaczewski, J., Nazarewicz, W., Werner, T. R., Berger, J. F., Chinn, C. R., & Dechargé, J. 1996, *Phys. Rev. C*, 53, 2809
- Eichler, D., Livio, M., Piran, T., & Schramm, D. N. 1989, *Nature*, 340, 126
- Fowler, W. A., Caughlan, G. E., & Zimmermann, B. A. 1967, *ARA&A*, 5, 525
- Freiburghaus, C., Kolbe, E., Rauscher, T., Thielemann, F.-K., Kratz, K.-L., & Pfeiffer, B. 1997, *Nucl. Phys. A*, 621, 405c
- Fukunishi, N., Otsuka, T., & Sebe, T. 1992, *Phys. Lett. B*, 296, 279
- Fuller, G., & Meyer, B. S. 1995, *ApJ*, 453, 792
- François, P., & Gacquer, W. 1998, in *Nuclei in the Cosmos V*, ed. N. Prantzos (Gif-sur-Yvette: Editions Frontières), in press
- Goriely, S. 1998, *Phys. Lett. B*, 436, 10
- Goriely, S., & Arnould, M. 1996, *A&A*, 312, 327
- . 1997, *A&A*, 322, L29
- Gratton, R. G., & Sneden, C. 1991, *A&A*, 241, 501
- Hilf, E. R., von Groote, H., & Takahashi, K. 1976, in *Proc. Third Int. Conf. on Nuclei Far from Stability* (CERN Rep. 76-13; Geneva: CERN), 142
- Hillebrandt, W., Takahashi, K., & Kodoma, T. 1976, *A&A*, 52, 63
- Hoff, P., et al. 1996, *Phys. Rev. Lett.*, 77, 1020
- Hoffman, R. D., Woosley, S. E., Fuller, G. M., & Meyer, B. S. 1996, *ApJ*, 460, 478
- Hoffman, R. D., Woosley, S. E., & Qian, Y.-Z. 1997, *ApJ*, 482, 951
- Howard, W. M., Goriely, S., Rayet, M., & Arnould, M. 1993, *ApJ*, 417, 713
- Ibbotson, R. W., et al. 1998, *Phys. Rev. Lett.*, 80, 2081
- Janka, H.-T., & Müller, E. 1996, *A&A*, 306, 167
- Käppeler, F., Beer, H., & Wisshak, K. 1989, *Rep. Prog. Phys.*, 52, 945
- Kolbe, E., Krewald, S., Langanke, K., & Thielemann, F.-K. 1992, *Nucl. Phys. A*, 540, 599
- Kratz, K.-L. 1995, in *AIP Conf. Proc. 327, Third Int. Conf. on Nuclei in Cosmos*, ed. M. Busso, R. Gallino, & C. M. Raiteri (New York: AIP), 113
- Kratz, K.-L., Bitouzet, J.-P., Thielemann, F.-K., Möller, P., & Pfeiffer, B. 1993, *ApJ*, 403, 216
- Kratz, K.-L., Pfeiffer, B., & Thielemann, F.-K. 1998, *Nucl. Phys. A*, 630, 352
- Kratz, K.-L., Thielemann, F.-K., Hillebrandt, W., Möller, P., Harms, V., & Truran, J. W. 1998, *J. Phys. G*, 14, 331
- Lalazissis, G. A., Vretenar, D., & Ring, P. 1998, *Phys. Rev. C*, 57, 2294
- Lattimer, J. M., Mackie, F., Ravenhall, D. G., & Schramm, D. M. 1977, *ApJ*, 213, 225
- Matthews, G. J., Bazan, G., & Cowan, J. J. 1992, *ApJ*, 391, 719

- Mayle, R. W., & Wilson, J. R. 1990, in Proc. 10th Santa Cruz Summer Workshop, Supernovae, ed. S. E. Woosley (Berlin: Springer), 333
- McWilliam, A., Preston, G. W., Sneden, C., & Searle, C. 1995, *AJ*, 109, 2757
- Meyer, B. S. 1989, *ApJ*, 343, 254
- , 1994, *ARA&A*, 32, 153
- Meyer, B. S., & Brown, J. S. 1997a, *Nucl. Phys. A*, 621, 409c
- , 1997b, *ApJ*, 112, 199
- Meyer, B. S., Mathews, G. J., Howard, W. M., Woosley, S. E., & Hoffman, R. D. 1992, *ApJ*, 399, 656
- Meyer, B. S., McLaughlin, G. C., & Fuller, G. M. 1998, *Phys. Rev. C*, 58, 3696
- Möller, P., Nix, J. R., & Kratz, K.-L. 1997, *At. Data Nucl. Data Tables*, 66, 131
- Möller, P., Nix, J. R., Myers, W. D., & Swiatecki, W. J. 1996, *At. Data Nucl. Data Tables*, 59, 185
- Nissen, P. E., Gustafsson, B., Edvardsson, B., & Gilmore, G. 1994, *A&A*, 285, 440
- Orr, N. A., et al. 1991, *Phys. Lett. B*, 258, 29
- Pearson, J. M., Nayak, R. C., & Goriely, S. 1996, *Phys. Lett. B*, 387, 455
- Pfeiffer, B., & Kratz, K.-L. 1996, *Kernchemie Rep.*, Univ. Mainz, unpublished
- Pfeiffer, B., Kratz, K.-L., & Thielemann, F.-K. 1997, *Z. Phys., A*, 357, 235
- Qian, Y.-Z., Haxton, W. C., Langanke, K., & Vogel, P. 1996, *Phys. Rev. C*, 55, 1532
- Qian, Y.-Z., Vogel, P., & Wasserburg, G. J. 1998, *ApJ*, 494, 285
- Qian, Y.-Z., & Woosley, S. E. 1996, *ApJ*, 471, 331
- Rauscher, T., Applegate, J. H., Cowan, J. J., Thielemann, F.-K., & Wiescher, M. 1994, *ApJ*, 429, 499
- Rauscher, T., Thielemann, F.-K., & Kratz, K.-L. 1997, *Phys. Rev. C*, 56, 1613
- Rosswog, S., Liebendörfer, M., Thielemann, F.-K., Davies, M., Benz, W., & Piran, T. 1999, *A&A*, 341, 499
- Sneden, C., McWilliam, A., Preston, G. W., Cowan, J. J., Burris, D. I., & Armosky, B. J. 1996, *ApJ*, 467, 819
- Sorlin, O., et al. 1993, *Phys. Rev. C*, 47, 2941
- Takahashi, K., Witt, J., & Janka, H.-T. 1994, *A&A*, 286, 857
- Thielemann, F.-K., Arnould, M., & Hillebrandt, W. 1979, *A&A*, 74, 175
- Thielemann, F.-K., Arnould, M., & Truran, J. W. 1987, in *Adv. Nucl. Astrophys.*, ed. E. Vangioni-Flam (Gif-sur-Yvette: Editions Frontières), 525
- Thielemann, F.-K., Bitouzet, J.-P., Kratz, K.-L., Möller, P., Cowan, J. J., & Truran, J. W. 1993, *Phys. Rep.*, 227, 269
- Thielemann, F.-K., et al. 1997, in *Capture Gamma-Ray Spectroscopy*, ed. G. Molnar (Budapest: Springer Hungarica)
- Thielemann, F.-K., Hashimoto, M., & Nomoto, K. 1990, *ApJ*, 349, 222
- Thielemann, F.-K., Kratz, K.-L., Pfeiffer, B., Rauscher, T., van Wormer, L., & Wiescher, M. C. 1994, *Nucl. Phys. A*, 570, 329c
- Thielemann, F.-K., Nomoto, K., & Hashimoto, M. 1996, *ApJ*, 460, 408
- van Wormer, L., Görres, J., Iliadis, C., Wiescher, M., & Thielemann, F.-K. 1994, *ApJ*, 432, 267
- Wasserburg, G., Busso, M., & Gallino, R. 1996, *ApJ*, 466, L109
- Witt, J., Janka, H.-T., & Takahashi, K. 1994, *A&A*, 286, 841
- Woosley, S. E., Arnett, W. D., & Clayton, D. D. 1973, *ApJS*, 26, 231
- Woosley, S. E., & Hoffman, R. D. 1992, *ApJ*, 395, 202
- Woosley, S. E., Wilson, J. R., Mathews, G. J., Hoffman, R. D., & Meyer, B. S. 1994, *ApJ*, 433, 229
- Zhang, C. T., et al. 1997, *Z. Phys. A*, 358, 9